

AD-A129 406

UNSTEADY TRANSONIC FLOW IN A TWO-DIMENSIONAL DIFFUSER:
INTERPRETATION OF..(U) MCDONNELL DOUGLAS RESEARCH LABS
ST LOUIS MO M SAJBEN ET AL. 31 MAR 82 MDC-Q0779

1/1

UNCLASSIFIED

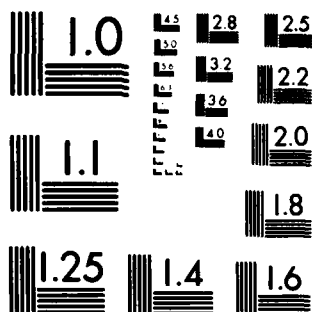
AFOSR-TR-83-0453 F49620-77-C-0082

F/G 20/4

NL

END
DATE
FILMED

7-83
DTIC



MICROCOPY RESOLUTION TEST CHART
NATIONAL BUREAU OF STANDARDS 1963-A

AD A129406

DTIC FILE COPY

MCDONNELL DOUGLAS RESEARCH LABORATORIES

DTIC

MCDONNELL DOUGLAS

CORPORATION

JUN 10 1959

A

88

103

UNCLASSIFIED

SECURITY CLASSIFICATION OF THIS PAGE (When Data Entered)

REPORT DOCUMENTATION PAGE		READ INSTRUCTIONS BEFORE COMPLETING FORM
1. AFOSR-MP- AFOSR-TR- 83-0453 100-00729	2. GOVT ACCESSION NO. AD-A129406	3. RECIPIENT'S CATALOG NUMBER
4. TITLE (and Subtitle) UNSTEADY TRANSONIC FLOW IN A TWO-DIMENSIONAL DIFFUSER: INTERPRETATION OF EXPERIMENTAL RESULTS		5. TYPE OF REPORT & PERIOD COVERED Scientific Report 1 April 1981-31 March 1982
7. AUTHOR(s) M. Sajben T. J. Bogar		6. PERFORMING ORG. REPORT NUMBER
9. PERFORMING ORGANIZATION NAME AND ADDRESS McDonnell Douglas Research Laboratories McDonnell Douglas Corporation St. Louis, MO 63166		8. CONTRACT OR GRANT NUMBER(s) F49620-77-C-0082
11. CONTROLLING OFFICE NAME AND ADDRESS Air Force Office of Scientific Research /NA Bolling Air Force Base, DC 20332		10. PROGRAM ELEMENT, PROJECT, TASK AREA & WORK UNIT NUMBERS 61102F 2307 /A4
14. MONITORING AGENCY NAME & ADDRESS (if different from Controlling Office)		12. REPORT DATE 31 March 1982
		13. NUMBER OF PAGES 75
		15. SECURITY CLASS. (of this report) Unclassified
		15a. DECLASSIFICATION/DOWNGRADING SCHEDULE
16. DISTRIBUTION STATEMENT (of this Report) Approved for public release; distribution unlimited.		
17. DISTRIBUTION STATEMENT (of the abstract entered in Block 20, if different from Report)		
18. SUPPLEMENTARY NOTES <div style="text-align: right;">A</div>		
19. KEY WORDS (Continue on reverse side if necessary and identify by block number) Transonic flow Air-breathing propulsion system Flowfield oscillations Internal flow		
20. ABSTRACT (Continue on reverse side if necessary and identify by block number) Experimental data obtained over a four-year period on transonic, oscillatory diffuser flows were examined and compared with the predictions of simple, one-dimensional theories. Acoustic theory, accounting for upstream- and downstream-propagating acoustic waves, correctly describes pressure perturbations in attached flows, provided the wave reflection process at the shock is properly modeled.		

DD FORM 1473
1 JAN 73

EDITION OF 1 NOV 65 IS OBSOLETE

UNCLASSIFIED

SECURITY CLASSIFICATION OF THIS PAGE (When Data Entered)

UNCLASSIFIED

SECURITY CLASSIFICATION OF THIS PAGE(When Data Entered)

→ Unsteady boundary layers strongly influence pressure perturbations in separated flows and velocity perturbations in both attached and separated flows, with the result that acoustic theory fails in these cases. The boundary layers display slow, transverse, downstream-moving waves (termed interface waves) that strongly influence the core flow velocity and pressure perturbations through displacement effects. The Eulerian velocity perturbations associated with this wave motion are large within the boundary layer.

A one-dimensional model was constructed, incorporating both acoustic waves and the interface wave. The model was found capable of qualitatively predicting the experimentally observed amplitude and phase-angle distributions in cases where acoustic theory fails. The results show that amplitude distributions are insensitive to the inclusion of interface waves: their effect is most evident in the phase-angle distributions and in the predicted natural frequencies. ←

It is believed that improved representations of the interface wave, when combined with empirical reflection coefficients and a core flow model accounting for streamwise cross-section variation, could lead to a relatively simple theory suitable for estimating oscillatory properties of transonic diffuser flows.

Acoustic Wave

DTIC

ONR

INSTRUMENT

2

DTIC

ONR

INSTRUMENT

2

A

UNCLASSIFIED

SECURITY CLASSIFICATION OF THIS PAGE(When Data Entered)

PREFACE

This report is based on research performed by the McDonnell Douglas Research Laboratories, St. Louis, Missouri, on unsteady transonic flows in two-dimensional diffusers. The research was conducted under Contract No. F49620-77-C-0082 for the Air Force Office of Scientific Research. The performance period was 1 April 1981 to 31 March 1982.

The work was performed in the Flight Sciences Department of MDRL under the supervision of Dr. Raimo J. Hakkinen. The principal investigator was Dr. Miklos Sajben; Dr. Thomas J. Bogar was co-investigator. The program manager was Dr. James D. Wilson, Air Force Office of Scientific Research.

This report has been reviewed and is approved.



R. J. Hakkinen
Director-Research
McDonnell Douglas Research Laboratories



D. P. Ames
Staff Vice President
McDonnell Douglas Research Laboratories

AIR FORCE OFFICE OF SCIENTIFIC RESEARCH (AFOSR)
NOTICE OF TRANSMITTAL TO DTIC
This technical report has been reviewed and is
approved for public release IAW AFR 190-12.
Distribution is unlimited.
MATTHEW J. KERPER
Chief, Technical Information Division

TABLE OF CONTENTS

	<u>Page</u>
NOMENCLATURE.....	1
1. INTRODUCTION.....	4
2. OBJECTIVES.....	8
3. STATISTICAL PROPERTIES OF SIGNALS.....	9
3.1 Frequency Content.....	9
3.2 Length Scales.....	14
3.3 One-Dimensional Models.....	15
4. ELEMENTARY WAVES.....	16
4.1 Acoustic Waves.....	17
4.2 Interface Waves.....	18
5. BOUNDARY CONDITIONS AT THE SHOCK.....	22
5.1 Acoustic/Acoustic Reflection.....	22
5.2 Acoustic/Interface Reflection.....	26
6. BOUNDARY CONDITIONS DOWNSTREAM.....	28
6.1 Open End.....	28
6.1.1 Acoustic/Acoustic Reflection.....	28
6.1.2 Interface/Acoustic Reflection.....	28
6.2 Externally Imposed Perturbations.....	29
6.3 End of Core Flow.....	29
7. OSCILLATIONS.....	31
7.1 Acoustic Oscillations.....	31
7.1.1 Energy Considerations.....	31
7.1.2 Solutions of the Acoustic Wave Equations.....	33
7.1.2.1 Natural Oscillations with Open Duct End.....	34

PRECEDING PAGE BLANK-NOT FILLED

TABLE OF CONTENTS (Continued)

	<u>Page</u>
7.1.2.2 Forced Oscillations.....	37
7.2 Oscillations Incorporating Interface Waves.....	41
7.2.1 Interface Oscillation.....	42
7.2.2 Compound Oscillations.....	46
8. RESONANCE.....	52
8.1 Resonance in a Mathematical Model.....	52
8.2 Resonance in a Real System.....	54
8.3 Extreme Amplitudes.....	56
9. SUMMARY AND CONCLUSIONS.....	58
REFERENCES	59
APPENDIX A: PRESSURE PERTURBATIONS IN INTERFACE WAVES.....	61
APPENDIX B: TREATMENT OF TIME-DEPENDENT LOCATION OF UPSTREAM BOUNDARY.....	66

LIST OF ILLUSTRATIONS

<u>Figure</u>	<u>Page</u>
1. Typical supercritical flow patterns.....	6
2. Power spectral density distributions of (a) shock displacement without excitation and (b) core flow total pressure fluctuations with excitation at 300 Hz.....	10
3. Power spectral density distributions of (a) shock displacement and (b) top-wall pressure fluctuations.....	11
4. Trends of shock displacement and top-wall static fluctuation (rms) intensities.....	13
5. Conjectured instantaneous transverse pressure distributions in interface waves at a fixed location, at time intervals of half period.....	20
6. Complex reflection coefficient at a plane, normal shock; (a) absolute value and (b) phase delay.....	24
7. Normalized shock displacement in response to downstream pressure perturbations; (a) amplitude and (b) phase delay.....	25
8. Amplitude and phase-angle distributions for an acoustic, natural oscillation with reflection coefficient magnitude (R) as parameter.....	36
9. Amplitude and phase-angle distributions for an acoustic, natural oscillation, with reflection coefficient argument (ϕ) as parameter.....	38
10. Amplitude distribution for a forced acoustic oscillation and its relation to the reflection coefficient.....	41
11. Amplitude and phase-angle distributions for a natural interface oscillation, with reflection coefficient magnitude (Q) as parameter.....	45
12. Regimes of compound oscillations and their relation to three experimental observations.....	46
13. Natural frequencies for compound oscillations ($k = 1$ to 5) and their relation to acoustic natural frequencies ($n = 1, 2$).....	48
14. Amplitude and phase angle distribution for compound natural oscillations, with Q as parameter.....	49

LIST OF ILLUSTRATIONS (Continued)

<u>Figure</u>	<u>Page</u>
15. Measured and theoretical streamwise distribution of amplitude and phase angle for the second harmonics of the fluctuations of midstream static pressure.....	51
16. Acoustic oscillation amplitudes detected at various locations in a constant-area channel as functions of excitation frequency.....	55
A-1. Analysis of spatial structure of pressure variations in interface waves.....	61
A-2. Instantaneous pressure distributions near an oscillating shock in a divergent channel.....	67

NOMENCLATURE

a	speed of sound
A	admittance ratio (Equation (7))
C	constant
E	acoustic energy per unit volume
f	frequency
F	amplitude of oscillation prescribed at downstream end
G	power spectral density
i	$\sqrt{-1}$
I	acoustic intensity per unit area
k	wave number
K	modified wave number (Equation (33))
L	streamwise length of channel ($x_e - x_o$)
M	Mach number
p	pressure
P	normalized pressure perturbation (Equation (29))
Q	reflection coefficient for interface wave
r	radius of curvature
R	reflection coefficient for acoustic wave
S	cross-sectional area
t	time
T	transmission coefficient
u	x-component of fluid velocity
v	phase velocity (Equation (5))
V	volume
U	normalized velocity perturbation (Equation (29))
w	interface wave speed in laboratory frame
W	$= w/a$
x	streamwise space coordinate, zero at time-mean shock position, positive towards subsonic flow
x_o	normalized shock displacement (Equation (12))
y	transverse space coordinate
Z	a complex number

α	= A_e/A_t area ratio of diffuser
γ	isentropic exponent (= 1.4)
δ	boundary-layer thickness
ϵ	amplitude of boundary-layer-thickness variation in interface wave
ϕ	argument of \tilde{R}
κ	wavenumber
λ	wavelength
μ	function defined by Equation (38b)
ν	function defined by Equation (41b)
ρ	fluid density
ψ	argument of \tilde{Q}
ω	angular frequency
Ω	= $\omega (\bar{a}_2^2 d \ln S/dx)_\sigma^{-1}$, normalized frequency

Subscripts

c	core flow
e	("exit") downstream end of channel
ex	excitation
i	imaginary part
g	geometric (area)
n,j,k	order of harmonics for acoustic, interface, and compound oscillations
m	defined in Equation (45)
max	maximum
p	pressure
s	static
t	throat
u	velocity
w	on wall
1,2	immediately before and after shock
σ	at time-mean shock position
+	downstream-moving acoustic wave
-	upstream moving acoustic wave
*	interface wave
(\sim)	complex quantity

Superscripts

- ($\bar{}$) time-mean
- ()' perturbation quantity
- ($\vec{}$) vector
- (\wedge) argument of complex number
- (\sim) distance normalized by throat height

1. INTRODUCTION

Motivated by the desire to improve theoretical flowfield prediction capabilities for the air inlets of supersonic propulsion systems, detailed experimental investigations of nominally two-dimensional, unsteady, transonic diffuser flows were performed at MDRL from 1977 to 1982 under sponsorship of Air Force Office of Scientific Research (AFOSR). The specific topics and results are summarized in the Final Technical Report.¹ This effort resulted in a large and systematic collection of data describing various aspects of both natural fluctuations and oscillations forced by externally imposed perturbations. Extensive documentation of the results is available.²⁻⁶

This data base is suitable for verification of related computer codes currently under development at several organizations (e.g., NASA Ames Research Center,^{7,8} Air Force Flight Dynamics Laboratories,^{9,10} and Scientific Research Associates under sponsorship of NASA Lewis Research Center), and has been used for such purposes.⁷⁻⁸

Apart from using the results as test cases for computational efforts, a parallel objective of the work was to identify and characterize the important physical processes and mechanisms governing the oscillations. Awareness of the underlying physics provides a rational basis for the judgments and compromises that must be made in the engineering development process, usually from incomplete information. Identification of the physical mechanisms is also essential for the creation of simple theoretical models, which can be invaluable in formulating objectives for experimental inquiries and providing a framework for presenting experimental results.

The present report describes the work performed during the last year of the AFOSR contract. The overall objective was to examine all available experimental information, relate the various measurements, and interpret results in terms of a consistent physical model. Special attention was given to selected problem areas (listed in Section 2) as being of critical importance. The material of this report is intended to serve as foundation for relatively simple theories of engineering utility.

The experimental information utilized is extensive, and its detailed review within this report would be prohibitively lengthy. Reasonable famil-

ilarity with References 2-5 and 11 is a prerequisite to the effective use of the present report.

The analysis is based on data obtained from two different diffuser models: one with an exit-to-throat area ratio (α) of 2.37 (model B, References 1-3 and 12) and another with $\alpha = 1.5$ (model G, References 4-6 and 11).

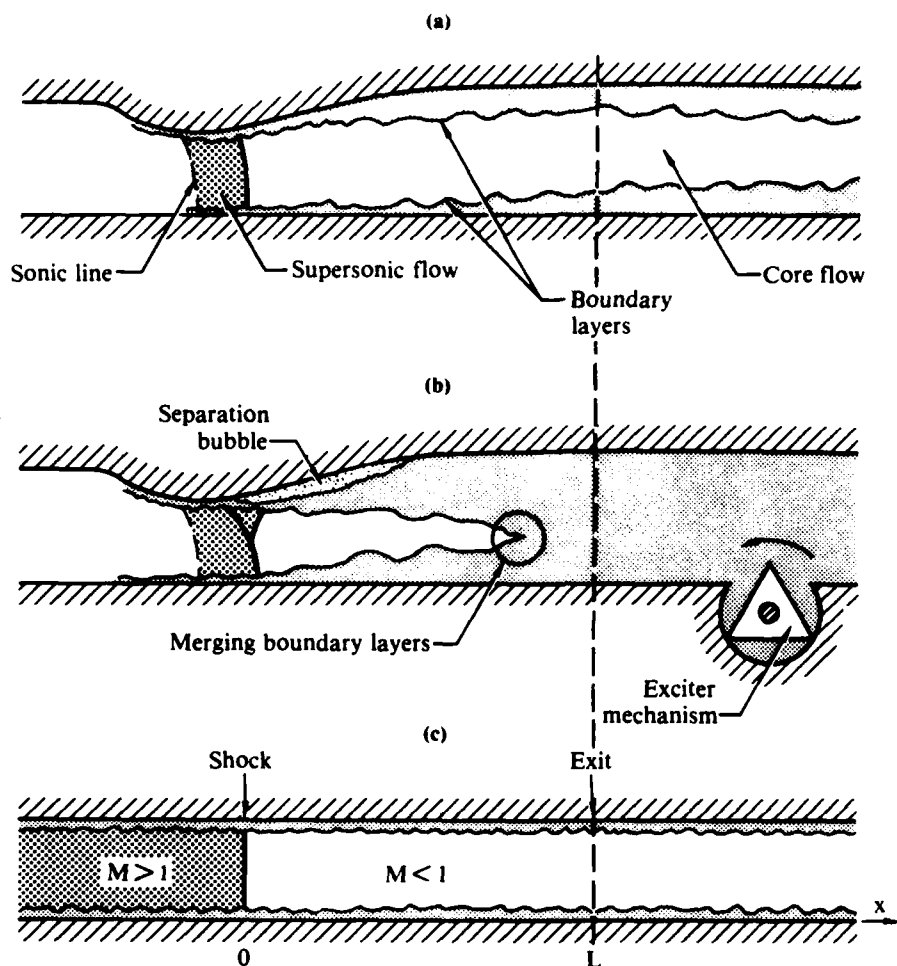
The flow in model B exhausted directly to the laboratory so that the boundary condition over the exit cross section was closely characterized as a spatially and temporally constant static pressure. Model G could be operated in the same way or its exit cross-sectional area could be modulated at frequencies up to 330 Hz using the rotary device shown in Figure 1b, thereby imposing an external, periodic perturbation on the flow.

The length of model G could be varied by mounting extension segments of various length at the downstream end. The distance from the time-mean shock location to the atmospheric exhaust was varied by this method from 14.4 to 30.5 throat heights.

The principal experimental parameter was the strength of the terminal shock, characterized by the time-mean Mach number immediately before the shock, at the edge of the top-wall boundary layer (M_o). M_o uniquely determined the structure of the time-mean flow in both models.

In model G, the boundary layers were attached everywhere for $M_o < 1.27$ (weak shock, no separation (NS)). For $M_o > 1.28$, the top-wall boundary layer separated at the foot of the shock, creating a separation bubble approximately four throat-heights long. This mode is referred to as strong-shock, or shock-induced separation (SIS). From $M_o = 1.27$ to 1.28 the flow displayed low-frequency, irregular, intermittent transitions between the NS and SIS modes. The mean flow remained the same in the presence of excitation; the excitation amplitude was too small for a nonlinear modification of the mean flow. The addition of duct segments to the downstream end left the flow in the upstream portion unaltered.

In model B the top-wall boundary layer was separated by the adverse pressure gradient well downstream of the shock (pressure-gradient-induced separation (PGIS)), for $M_o < 1.3$. For stronger shocks, SIS occurred as in model G.



GP21-0922-1

Figure 1. Typical supercritical flow patterns: (a) unexcited diffuser flow with no separation (weak shock), (b) excitation of diffuser flow with shock-induced separation (strong shock), and (c) constant area theoretical model.

The Reynolds number based on throat height was approximately one million for all cases. Since the dominant top-wall boundary layer was tripped and turbulent, no significant Reynolds number effects were expected or found.

In unexcited flows, all flow properties displayed spontaneous oscillations. The shock displacement fluctuations were always confined to frequencies below 300 Hz, and the associated power spectral density (PSD) curves displayed well-defined peaks. The frequencies associated with the peaks were defined as the natural frequencies of the system. One to three of these were observed, depending on the (M_0 , L) combination.

The exciter was used in model G only and always in conjunction with the shortest channel length, and the excitation frequency range extended from 10 to 330 Hz. The independent test parameters in the forced-oscillation runs thus were M_σ and f_{ex} . The excitation amplitudes, as measured by the pressure fluctuation amplitude at a selected, nominal exit station ahead of the exciter were small, always below 2% of the local static pressure.

Figure 1a illustrates a weak-shock flow without excitation, and Figure 1b is a strong-shock flow with excitation. Figure 1c shows a constant-area idealization of the flow, to be used later in discussing certain aspects of the oscillations.

The principal measured dynamic quantities were the shock position, static pressures at eight locations on the top wall, and total static pressures in the core flow over a streamwise range $\tilde{x}_\sigma < \tilde{x} < 8.1$. In a past MDC-funded study, the horizontal velocity components were also determined throughout the subsonic flowfield for three selected (M_σ , f_{ex}) combinations¹¹; data from this source also will be used in this analysis for comparisons.

2. OBJECTIVES

The objectives for the fifth contract year reported here were:

1. Characterize the intermittency observed between attached and separated flow modes at intermediate shock strengths and the effects of this phenomenon on the shock position and surface-pressure power spectra.
2. Determine the character, amplitude, and phase of the wave reflected from the shock/boundary-layer interaction region in response to the arrival of an acoustic wave from downstream.
3. Characterize the oscillation intensity of the overall flowfield and the amplitude of the excitation in a practical, measurable manner. Determine the forcing frequencies resulting in peak oscillation intensity (resonance), and relate these to the natural frequencies.

3. STATISTICAL PROPERTIES OF SIGNALS

3.1 Frequency Content

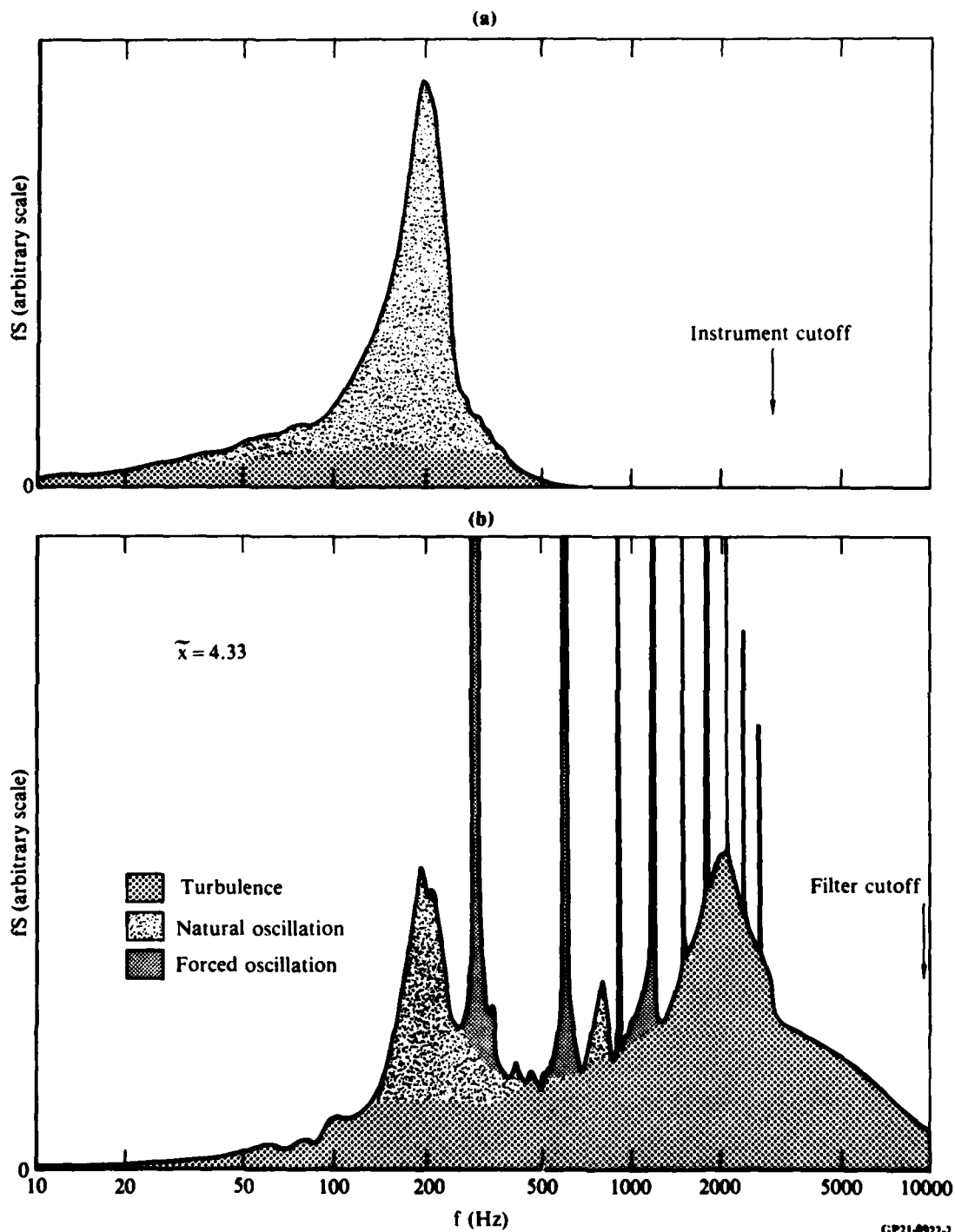
Numerous power-spectral density (PSD) distributions of shock position and pressure signals were generated for a variety of (M_o , f_{ex} , L) combinations and sensor locations. Selected examples will be presented of fS as a function of $\log_{10}f$, which have the property that the area under the curve for a given spectral band is directly proportional to the energy contained within that band, thereby facilitating recognition of important frequency ranges. The horizontal scale is terminated at 10 kHz, which was the bandwidth of the pressure measurement system. The shock position measurement system had a flat response to 4 kHz.

The shock-displacement PSD's have a relatively simple structure in all unexcited cases (Figures 2a and 3a). The fluctuations are confined below 300 Hz, and the principal features are well-defined peaks. One to three peaks were found in weak shock cases and always one peak in strong shock flows. The peaks are clearly defined but have a significant width, indicating that the motion is only approximately periodic. In excited flows the PSD is dominated by a single, sharp peak at the excitation frequency with a peak height greater than those associated with the higher harmonics and the natural fluctuation background.

The PSD's of pressure signals for all flow conditions and sensor locations are more complex than those for shock displacement.

A typical PSD of a total pressure signal in model G, for SIS mode with 300 Hz excitation (Figure 2b) illustrates that contributions to the total fluctuation energy come from three different sources:

- (a) **Natural fluctuations**, represented by the peak at 196 Hz, which is the frequency where the unexcited shock displacement PSD has its only peak.
- (b) **Boundary-layer turbulence**, represented in the figure by broadband contributions from approximately 400 Hz to 10 kHz and probably beyond. This contribution peaks at about 2 kHz for this particular PSD.
- (c) **Forced oscillations**, represented by the group of sharp peaks, at the excitation frequency and at its higher harmonics. Harmonics up to the 9th can be observed, indicating that the waveforms of the forced pressure fluctuations may be quite distorted.



GP21-4922-2

Figure 2. Power-spectral density distributions of (a) shock displacement, (b) core flow total pressure fluctuations with excitation at 300 Hz. Model G, $M_\infty = 1.353$.

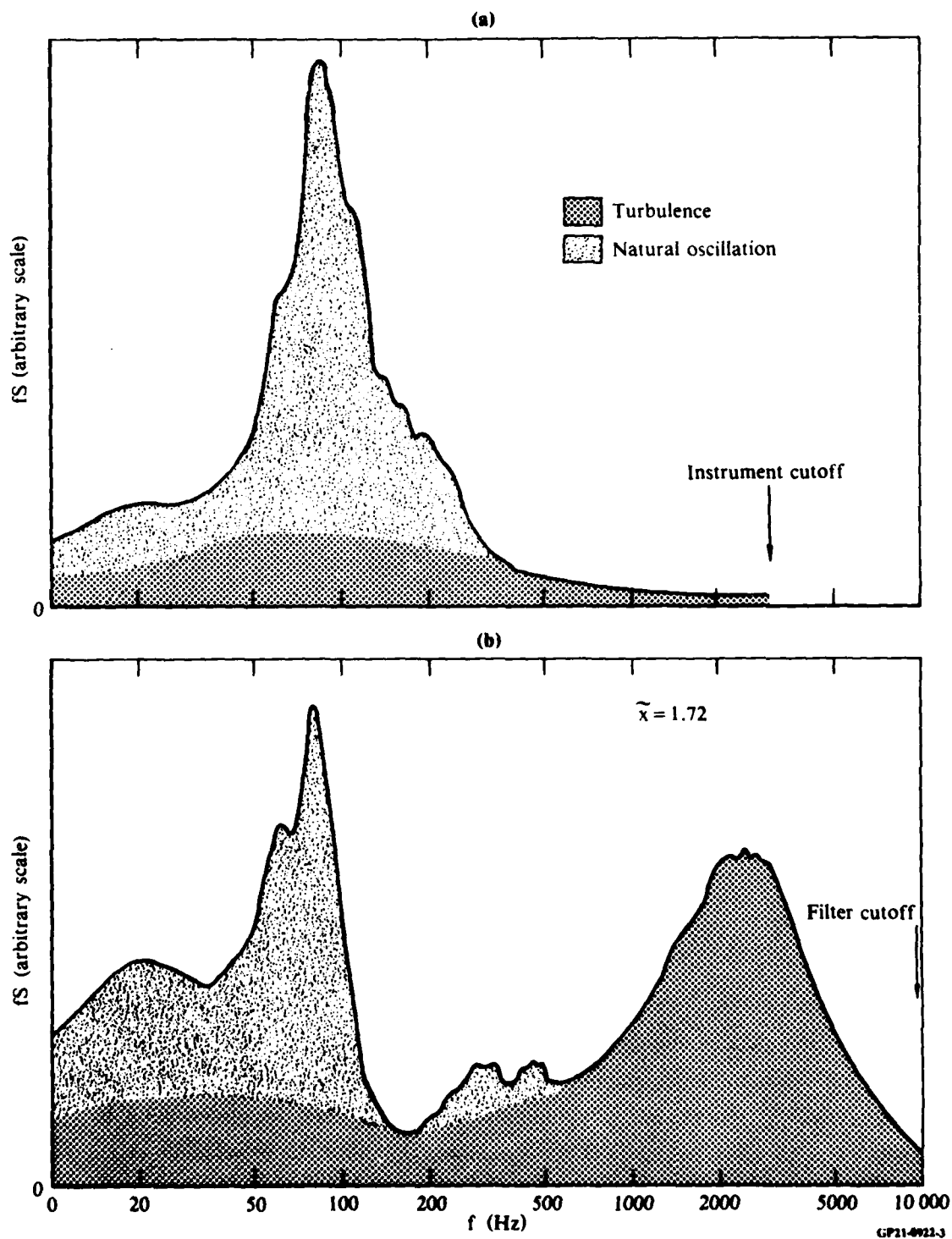


Figure 3. Power-spectral density distributions of (a) shock displacement and (b) top-wall pressure fluctuations. Model B, $M_o = 1.20$, no excitation.

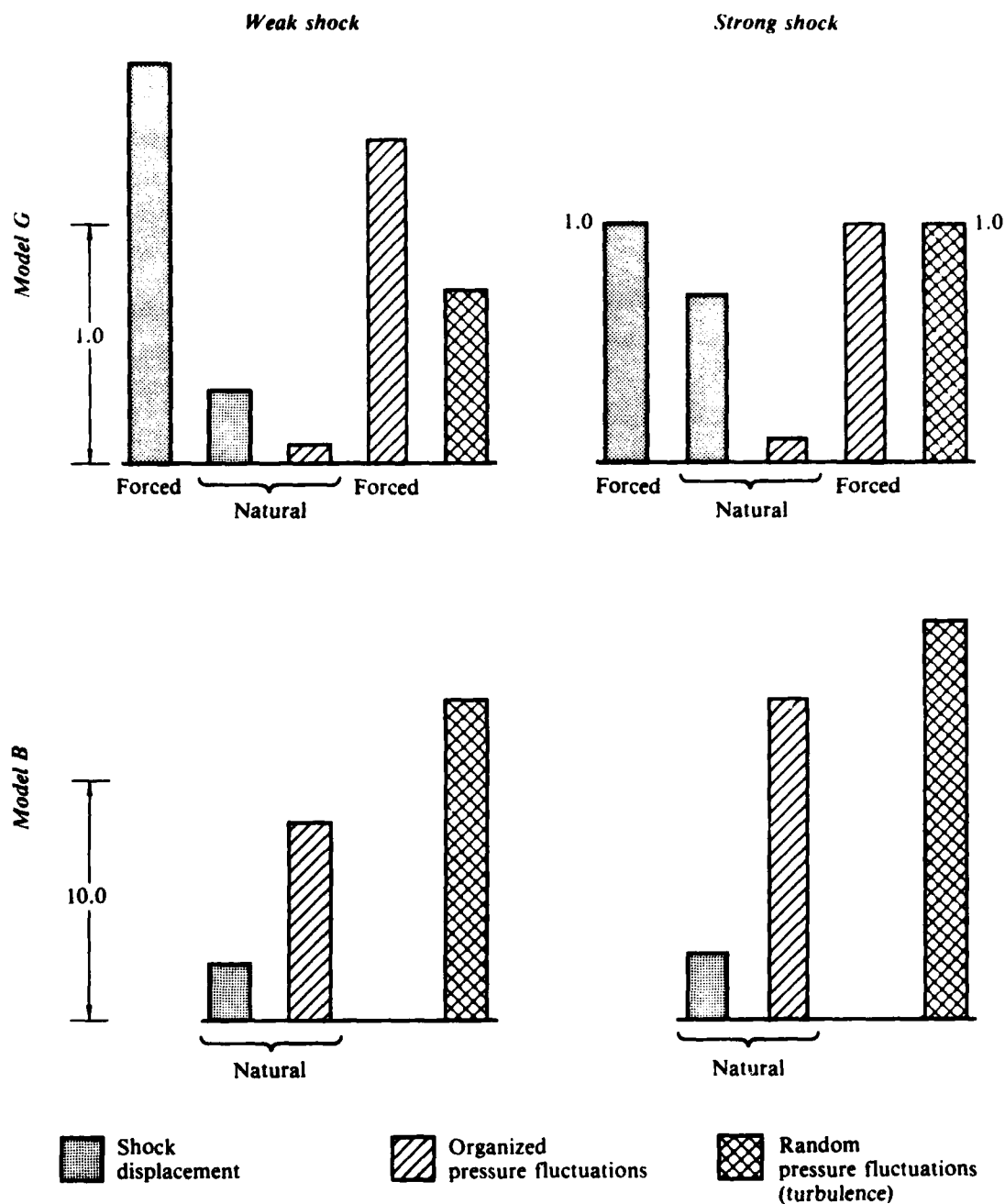
The relative magnitudes of the three contributions depend on the model, the flow conditions, and the location of the sensor.

Contributions from forced oscillations are controlled experimentally by changing the area modulation amplitude and are easily identified by ensemble-averaging. In general, contributions of forced oscillations were dominant in the case of weak shocks and comparable to random contributions in case of strong shocks. They were completely absent from all model B experiments. Figure 3b is an illustration of a wall pressure spectrum in an unexcited model B flow, PGIS mode.

Natural pressure oscillations are identified by distinct spectral peaks, but the quantization of their contribution is not straightforward, and no formal procedures were attempted to separate their contributions from turbulence. The shadings in Figures 2 and 3 are intended to emphasize the existence of two different mechanisms; the boundary between them is based on judgment only and not on any quantitative interpretation of the data. The relative intensity of natural oscillations in comparison to turbulence is a property of the flow and could not be controlled in the present experiments.

Figure 4 is a bar chart illustrating the observed trends in shock displacement and static-pressure fluctuation intensities for weak/strong shocks and models G/B. In each case, the intensities were normalized by the intensity observed in model G under strong-shock conditions. The bar heights are typical values, meant to illustrate overall trends; actual data may differ significantly depending on the precise flow conditions. The following points are made in connection with Figure 4:

- (a) The natural pressure-oscillation intensities are an order of magnitude higher in model B.
- (b) The natural shock oscillations are also greater in model B, but not in the same proportion as the pressures. The ratio of shock and pressure amplitudes is much less in model B; the shock in this model thus is less sensitive to pressure perturbations. The sensitivity reduction is attributed to the greater rate of area increase (for reasons discussed in Section 5.1).
- (c) Pressure and shock oscillation amplitudes both increase with shock strength.
- (d) Turbulence is a significant or major contributor to pressure fluctuations, but only the low-frequency portion influences shock motion.



GP21-4922-4

Figure 4. Trends of shock displacement and top-wall static pressure fluctuation (rms) intensities. Intensities for model G, strong-shock case are chosen as units. Actual values vary with flow condition; bar heights given are intended for order-of-magnitude guidance only. Note difference in scales between models.

In case of weak shocks, the static and total pressure PSD's taken in the core flow show comparable natural oscillatory contributions. In strong-shock flows, however, the natural frequency peaks are shown more clearly by the total pressure spectra than by the static pressure spectra. This result suggests that velocity perturbations play a larger role in the oscillations when the shock is strong, a conclusion that is supported by other sources of information (Section 4.2).

Interactions between the excitation and turbulence are minimal, even though the higher harmonics of the excitation frequency are comparable to the turbulence frequencies. This observation is supported by LDV data, which show that the magnitude and spatial distributions of all nonperiodic fluctuations (i.e., turbulence plus natural oscillations) are the same for excited and unexcited flows, other parameters being equal. These two fluctuation modes thus appear to coexist without mutual interference.

The interaction between excitation and natural frequencies also appears to be limited. Contrary to expectations, no particularly striking resonance behavior exists when the excitation frequency is equal to any one of the natural frequencies. This apparent discrepancy prompted additional inquiries (Section 2, Task 3) whose conclusions will be presented in Section 8.

3.2 Length Scales

Space-time correlations of shock displacement and pressure signals of all types, obtained for several unexcited flows in both models, indicate high correlation over streamwise distances comparable to the overall length of the diffuser.¹² In the case of forced oscillations, the forced oscillatory contribution is coherent over the entire flowfield; streamwise amplitude distributions of pressure and velocity fluctuations, obtained from ensemble-averaged data, show a high level of organized behavior from the shock to the exciter.⁵ The systematic behavior is found for all (M_σ , f_{ex}) combinations.

These observations establish the conclusion that large streamwise length scales distinguish the natural and forced oscillations from turbulence, which is generally associated with correlation distances of the order of the boundary-layer thickness.

3.3 One-Dimensional Models

Simple theoretical models permitting crude but rapid estimates of the principal oscillatory features are of considerable utility, provided their limitations are understood and taken into consideration. In light of the foregoing results, some of the assumptions implicit in using unsteady, quasi-one-dimensional, inviscid, linearized models^{13,14} become evident.

The neglect of turbulence contributions is clearly a major assumption, justifiable only in the low-frequency range where the turbulent fluctuations do not interact strongly with the overall oscillations. Turbulent fluctuations may, however, provide a sufficiently high perturbation level in the low-frequency range to excite large-scale oscillations, if they are unstable or associated with low damping.^{2,3} Removal of turbulence from the model precludes the possibility of predicting the amplitude of such oscillations.

Forced oscillations are represented by sharp peaks in the spectra and can be treated justifiably as single-frequency oscillations. Natural oscillations are only approximately periodic, presumably because they represent a selective response to the broadband excitation environment provided by turbulence. They too can be modeled as a single-frequency oscillation, although expectations concerning the prediction quality should be lower in comparison to fixed-frequency excitation cases.

Quasi-one-dimensional models thus have a reasonable promise of being able to predict some aspects of low-frequency, longitudinal oscillations, such as natural frequencies and shock displacement amplitudes for given pressure stimuli. However, the model cannot predict total pressure losses (dissipation) nor any oscillation property dependent on those losses, such as amplitudes associated with natural oscillations. Being one-dimensional, the model is inherently unsuitable for the prediction of transverse distributions (distortion) at the diffuser exit.

4. ELEMENTARY WAVES

The observed oscillatory patterns, whether forced or natural, are sustained by waves propagating and reflecting within the channel. The present studies of these patterns indicate that two types of elementary waves are present. One type is the well-known acoustic wave; in general, both the upstream- and downstream-propagating waves are evident. There is also overwhelming evidence that the boundary-layer/core-flow interface supports transverse, traveling waves similar to the Tollmien-Schlichting waves encountered in perturbed laminar boundary layers. The waves observed in these experiments propagate in initially turbulent boundary layers, and their properties, known only to a limited extent, may differ from the laminar waves in various ways. The possibility of different behavior is emphasized here by using the term interface waves for the observed waves.

When appropriate, waves will be treated in one-dimensional terms, describing sinusoidal time-dependence in terms of complex exponentials. A complex number, \tilde{z} , will be described either in terms of its real and imaginary part, or as an exponential expression containing the absolute value and an argument. The following notation will be used:

$$\tilde{z} = z_r = iz_i = ze^{i\hat{z}}. \quad (1)$$

The physically observable quantity is the real part, z_r . The properties considered are generally functions of x and t , and will appear in one of the following forms:

$$\tilde{z}(x, t) = g(x)e^{-i\omega t} = [g(x)e^{i\hat{g}(x)}]e^{-i(\omega_r + i\omega_i)t} \quad (2)$$

or

$$\tilde{z}(x, t) = [g(x)e^{\omega_i t}]e^{-i[\omega_r t - \hat{g}(x)]}, \quad (3)$$

where $g(x)$ and $\hat{g}(x)$ are the spatial distribution of amplitude and phase angle, respectively. The bracketed expression in the exponent of Equation (3) is used to define a phase velocity (v) as the velocity of an observer for whom the bracketed quantity appears to be constant, and thus the condition

$$[\omega_r t - \hat{g}(x)] = \text{const} \quad (4)$$

is satisfied locally. In differential form:

$$v \equiv \left(\frac{dx}{dt} \right)_{[\] = \text{const}} = \omega_r \left(\frac{d\hat{g}}{dx} \right)^{-1}. \quad (5)$$

The phase velocity represents the local speed of propagation of net perturbations; it is generally a function of x .

4.1 Acoustic Waves

The channels used in these experiments were slender without abrupt area changes, and the pressure fluctuations were small compared with the local static pressure. It is therefore reasonable to think of acoustic waves as having nearly planar wave fronts normal to the flow direction and propagating everywhere at the local speed of sound with respect to the fluid. The one-dimensional description implies that waves can propagate either upstream or downstream, but not in the transverse direction. The time-mean flow properties (velocity and pressure) depend on the streamwise coordinate, but this dependence will be neglected in the discussion of certain selected aspects of the oscillatory behavior.

Acoustic waves are, by definition, isentropic, involving concurrent variations of both pressure and velocity. The relation between the two is given by

$$p'_\pm = \pm \bar{\rho} a \tilde{u}'_\pm, \quad (6)$$

where the + and - signs apply to downstream- and upstream-moving waves, respectively.

In general, both wave families are present at any given location. The relation between them can be conveniently characterized by the admittance ratio, defined as

$$\tilde{A} = \frac{\bar{\rho} \tilde{a} \tilde{u}}{\tilde{p}} = \bar{\rho} \tilde{a} \left(\frac{\tilde{u}_+ + \tilde{u}_-}{\tilde{p}_+ + \tilde{p}_-} \right) . \quad (7)$$

The admittance ratio is a function of position only. The argument of \tilde{A} is the phase angle of the (net) local velocity perturbation with respect to the (net) local pressure perturbation.

4.2 Interface Waves

Forced oscillation experiments with strong shock flows produced extensive evidence of transverse displacements of the boundary-layer/core-flow interface that form a traveling wave moving downstream.

The properties of the interface wave differ drastically from those of acoustic waves. Interface waves are initiated by shock-displacement oscillations, associated with concurrent variations of the shock strength. The combination of time-dependent shock position and strength modulates the post-shock boundary-layer properties, which are then convected downstream forming the interface wave. The motion is maintained by and superimposed on the time-mean wall shear layer. Since convection is an essential part of the mechanism, the wave can travel only downstream. The average phase velocity of the wave (in the present experiments) is well below the local core flow speed, i.e., much less than the speed of a downstream acoustic wave.

The most detailed documentation of this wave is given in terms of LDV measurements for a strong-shock flow excited at 300 Hz.¹¹ In this case interface waves were on both the top- and bottom-wall boundary layers. The two waves were 180° out of phase, i.e., a thickening on the top was associated with thinning at the bottom, at all locations. The velocity asymmetry may have been caused by the asymmetric nature of the excitation method. LDV data show that the structure of the velocity perturbations is inherently two-

dimensional (in the two-dimensional mean flow of the experiment), in contrast to the nearly planar acoustic waves. Since the wave motion directly involves the boundary layers, the velocity fluctuations are especially intense in the outer regions of the layers.

Time-dependent pressures were measured on both walls and at one intermediate height within the core flow. These data suggest that the actual spatial distribution of the pressure perturbations is a weaker function of y (i.e., it is more nearly one-dimensional) than the velocity perturbation field.

The spatial structure of the pressure field is analyzed in Appendix A on the basis of displacement and streamline curvature considerations. According to the estimates, the streamwise pressure variation in the core flow is determined by the instantaneous displacement-thickness distribution. Since the Mach number of the core flow is high, relatively small displacement-thickness variation is sufficient to induce significant pressure variations. The model implies that pressure and velocity perturbations are 180° out of phase, in agreement with experiment and in conflict with acoustic theory.

Transverse pressure variations exist across both boundary layers, because of streamwise curvature effects. As shown in Appendix A, these variations are proportional to the product of $\bar{\delta}\delta'$ and are therefore larger on the top wall where both $\bar{\delta}$ and δ' are large. As illustrated in Figure 5, the curvature contribution on the top wall is in phase with the core flow perturbation, thereby explaining why fluctuations measured on the top wall are greater than those in a core flow. Figure 5 also illustrates how the small curvature contribution on the bottom wall permits the top and bottom pressure perturbations to be in phase (as found experimentally), despite the fact that the velocity perturbations are 180° out of phase.

The relation between the velocity and pressure fields is more complex than the simple connection given in Equation (6) for acoustic waves. Within the core flow, the pressure and velocity fluctuations are of the same order, but in the boundary layers, the (Eulerian) velocity perturbations are greater than those of an acoustic wave for the given pressure perturbation.

The pressure and velocity fluctuations estimated in Appendix A permit the calculation of an admittance-like quantity for the core flow, A_* (Equation

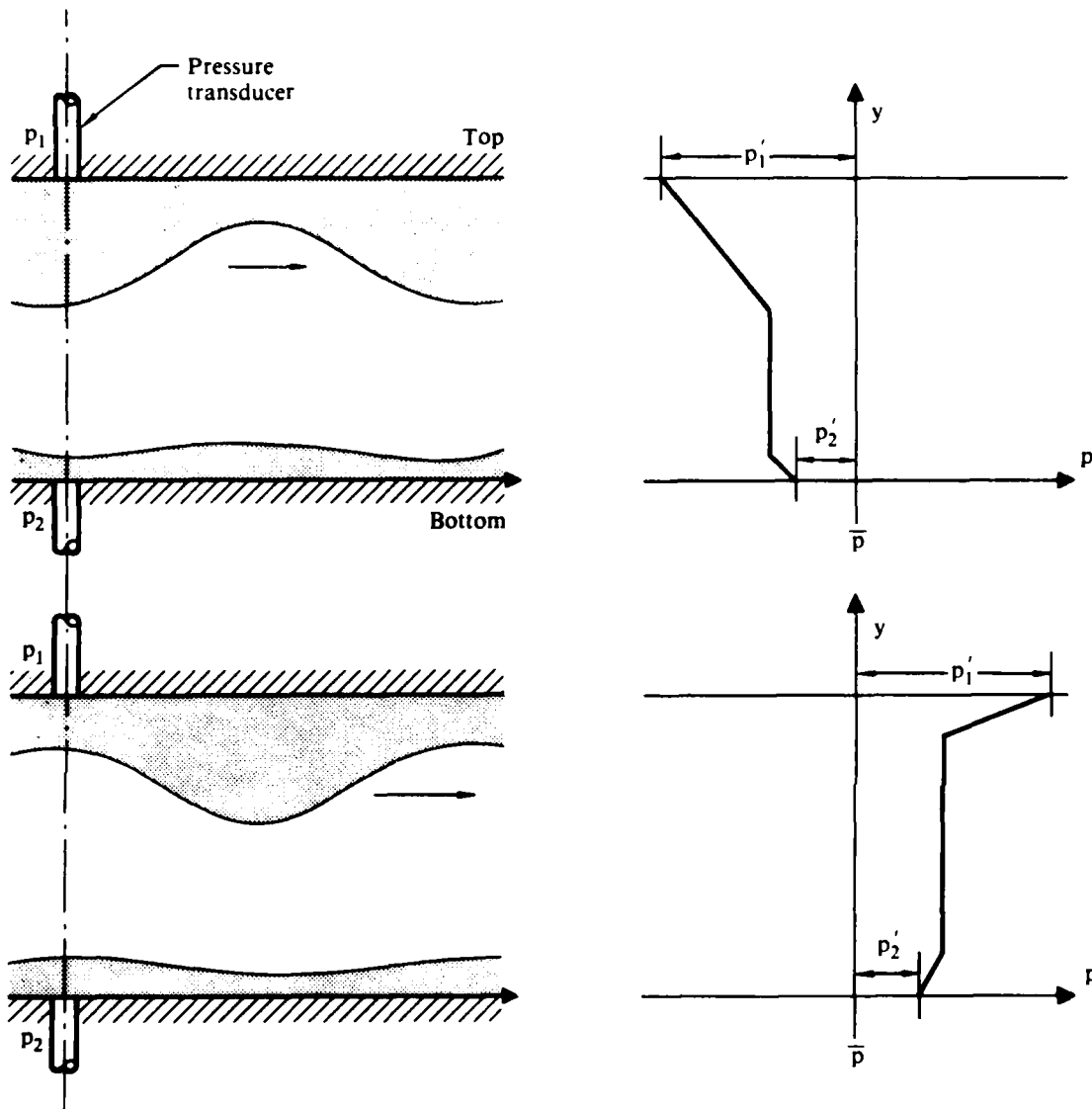


Figure 5. Conjectured instantaneous transverse pressure distributions in interface waves at a fixed location, at time intervals of a half-period. The sign of the pressure gradient within each layer corresponds to the sign of streamline curvatures. The interface waves on the two walls are out of phase by π , but the pressure variation seen by the top and bottom transducers are in phase.

GP21-4922-5

(A-11)) in the manner done for acoustic waves (Equation (7)). A_* is of the order unity, in agreement with data. If the admittance calculation were based on perturbations existing within the boundary layer, its values would be in the range 10-30, in agreement with experimental trends.

Interface wave amplitudes must have a definite upper limit since both $\bar{\delta}$ and ϵ are constrained to some fraction of the local channel height. The pressure perturbations associated with interface waves in slender channels are thus limited to relatively modest values (several percent of the local static pressure). In contrast, the amplitude of longitudinal waves associated with forced oscillations is determined by the externally imposed excitation level, with no obvious limitations. It seems therefore possible that interface waves may be unimportant not only for weak shock flows but also for strong shocks, provided the amplitude of the external excitation is sufficiently large.

Detailed measurements are available only for streamwise distances comparable to one wavelength of the interface wave. Under these conditions, it is difficult to establish any rate of change of amplitude. The amplitudes of the undulations appear to increase in the streamwise direction, but the thickness of the boundary layer and most other mean flow properties also vary, with the result that no statement can be made concerning the growth (or damping) rates of interface waves in the observed mean flow.

At the current level of understanding, it appears worthwhile to experiment with one-dimensional models of the interface waves, disregarding their inherent two-dimensionality and describing them with the same formalism of complex numbers as that used for acoustic waves (Section 4). It is emphasized, however, that pressure and velocity perturbations are not related by Equation (6), and only a single, downstream-moving family of waves exists, moving with some phase velocity $\bar{w}(x) < \bar{u}(x)$. Quantities associated with a one-dimensional interface-wave model will be designated by the subscript $(*)$.

5. BOUNDARY CONDITIONS AT THE SHOCK

5.1 Acoustic/Acoustic Reflection

The arrival of an upstream-propagating, plane acoustic wave at the shock (assumed also plane and normal) will create a reflected wave propagating in the opposite, downstream direction. For sinusoidal waves, this reflection process can be described by a complex reflection coefficient \tilde{R} , defined as

$$\tilde{R} = \left[\frac{p_+}{p_-} \right]_{\sigma} = Re^{i\phi}. \quad (8)$$

By virtue of Equation (3), \tilde{R} also describes the reflection of the velocity perturbations:

$$\tilde{R} = \left[-\frac{u_+}{u_-} \right]_{\sigma}. \quad (9)$$

Positive ϕ values indicate that the reflected wave is delayed with respect to the incident wave. The reflection coefficient is uniquely related to and is equivalent to the admittance ratio at $x = 0$. Using Equations (6), (7), and (8),

$$\tilde{R} = \frac{1 + \tilde{A}}{1 - \tilde{A}} \quad (10)$$

and

$$R = \left[\frac{(1 + A_r)^2 + A_1^2}{(1 - A_r)^2 + A_1^2} \right]^{1/2}. \quad (11)$$

Specification of \tilde{R} is a homogeneous boundary condition: if satisfied by some $p'(x,t)$, then it is also satisfied by $Cp'(x,t)$, where C is any constant.

The reflection coefficient for plane acoustic waves reflecting from a plane normal shock in a mildly varying area channel was derived by Culick.¹⁴ The analysis makes use of the fact that the normal shock relations are valid at any instant across the shock, even if it is in motion. The calculated reflection coefficients (after correction of minor errors in Reference 14) are given in Figure 6. The absolute values of \tilde{R} are small; for the condition of the present experiments, they are always below 1%. Thus a plane, normal shock represents a virtually anechoic termination. Figure 6b shows that the streamwise area change introduces a phase delay that increases with frequency and decreases with the rate of area change.

In addition to triggering a reflected wave, the arrival of a sound wave to the shock also causes shock displacement. The formulation of Reference 14 was used to calculate the shock displacement as function of the shock Mach number and the frequency in the following normalized form:

$$\tilde{x}_\sigma = \frac{\bar{p}_2}{p_2'} \left(\frac{d \ln S}{dx} \right)_\sigma \tilde{x}_\sigma = f(\bar{M}_\sigma, \Omega), \quad (12)$$

where p_2' is the amplitude of pressure oscillations immediately downstream of the shock. The results, given in Figure 7, show that the displacement amplitude decreases sharply as the frequency exceeds a relatively low cutoff value, approximated as

$$f \approx \frac{\bar{a}_2}{2\pi} \left(\frac{d \ln S}{dx} \right)_\sigma. \quad (13)$$

The shock displacement thus behaves as a low-pass-filtered version of post-shock pressure fluctuations. The pressure fluctuation spectrum created by the thick, highly turbulent boundary layers in the subsonic region usually contains large contributions above the frequency given by Equation (13), but

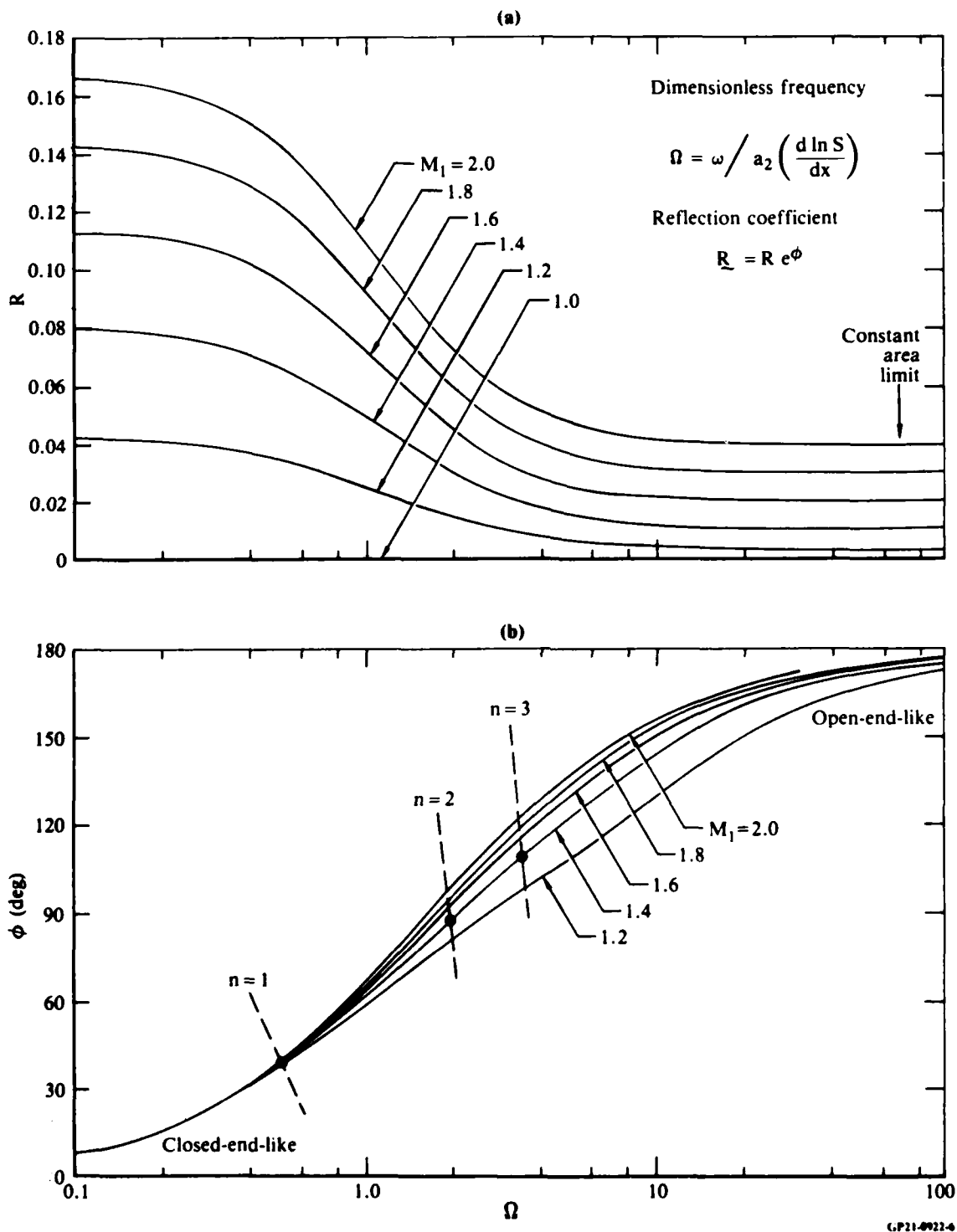


Figure 6. Complex reflection coefficient at a plane, normal shock: (a) absolute value and (b) phase delay. Dashed lines indicate the $\phi(\Omega)$ relations for natural oscillations in a constant area channel (Section 7.1).

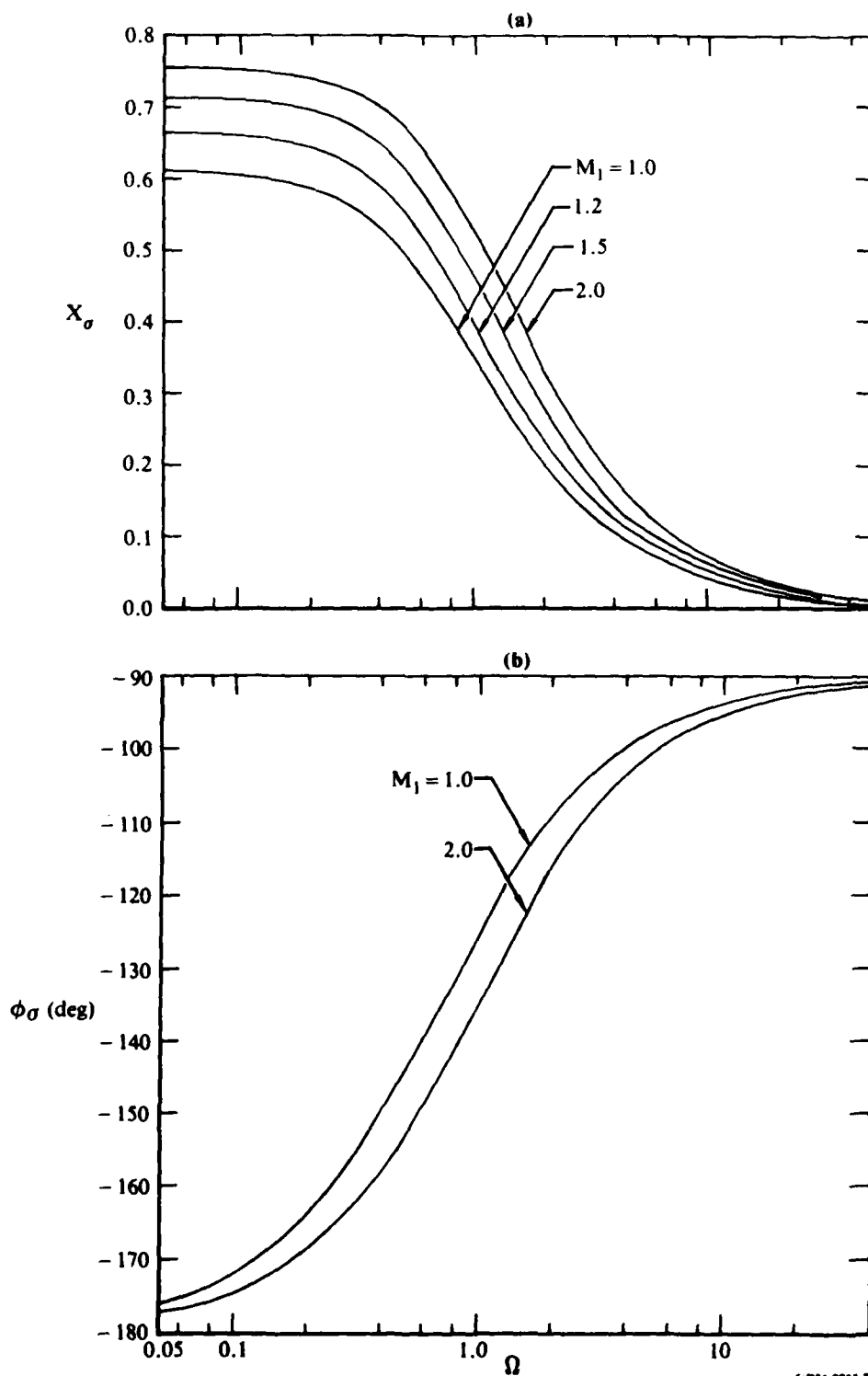


Figure 7. Normalized shock displacement in response to downstream pressure perturbations: (a) amplitude and (b) phase delay. Amplitude plot shows that the shock is to insensitive to high-frequency perturbations, negative delays indicate that the shock leads pressure fluctuation.

these fluctuations will not cause intense shock movements. The selective sensitivity of the shock is responsible for the significant differences between the shock displacement and pressure spectra, as illustrated in Figures 2 and 3.

Figures 6 and 7 both indicate that the participation of the shock in the overall oscillations becomes less significant as the frequency increases; both the reflected wave strength and the shock displacement amplitudes diminish rapidly beyond the cutoff frequency. Conversely, the absence of reflection at high frequencies prevents the organization of high-frequency disturbances into an oscillatory pattern encompassing the entire flowfield.

Appendix B contains a discussion of shock-strength dependence on shock speed, along with the problems of treating the time-dependent upstream boundary represented by the shock.

These computations assume that the terminal shock is a plane, normal shock. It is well known that strong shocks are configured as a lambda pattern, the reflection from which would be necessarily nonplanar. The separation bubble and its bounding free shear layer would also respond to the arrival of a sound wave in some unknown fashion. Strong-shock reflections thus differ drastically from their weak-shock counterpart, as do the respective oscillatory patterns. No analytical study of this process is available, and no experimental work appears to have been focused on it.

5.2 Acoustic/Interface Reflection

The arrival of an acoustic wave to the shock perturbs the strength and location of the shock, which in turn perturbs the properties (thickness) of the post-shock boundary layer. The perturbed thickness then initiates a displacement wave that emanates from the vicinity of the shock foot. The details of the process are complex, especially if the shock is strong. However, compared to the length of the channel, the phenomenon is local and may be conveniently viewed as a reflection process in which an incident acoustic wave creates a reflected interface wave, in addition to the already discussed acoustic reflection. Experimental data suggest that the absolute value of such a reflection coefficient is large, possibly in excess of unity.

In the spirit of linearized, one-dimensional theory, the acoustic/ interface reflection can be characterized by a complex reflection coefficient, Q . Noting that the velocity and pressure perturbation fields of the interface wave are related differently than those in acoustic waves, separate reflection coefficients need to be defined for pressure and velocity:

$$p'_+ = Q_p p'_- \quad (14)$$

$$u'_+ = Q_u u'_- \quad (15)$$

Experimental data suggest that Q_p and Q_u depend strongly on the shock strength. Precise values are not known, but trends of absolute values, inferred from model G data, are as follows:

	R	Q_p	Q_u
Weak shock	$\ll 1$	$R < Q_p \ll 1$	$R < Q_u < 1$
Strong shock	≈ 1	≈ 1	> 1

As mentioned in Section 4.2, the interface wave amplitudes may be limited because the associated transverse motions cannot become too large in slender channels. Therefore the linear Equations (14) and (15) apply only to small amplitudes, and that both Q_p and Q_u are nonlinear, decreasing functions of p'_- beyond a certain p'_- amplitude.

6. BOUNDARY CONDITIONS DOWNSTREAM

In the experiments conducted under this contract, two different downstream boundary conditions were used: simple open-end or periodic area modulation. The characterizations of the two differ considerably.

6.1 Open End

6.1.1 Acoustic/Acoustic Reflection

The arrival of a downstream-moving acoustic wave results in the reflection of an upstream acoustic wave, the process being described by a complex reflection coefficient \tilde{R}_e :

$$\tilde{R}_e = \frac{p'_-}{p'_+} = - \frac{u'_-}{u'_+} . \quad (16)$$

The classical condition for an open end is constant pressure (zero perturbation amplitude), which occurs if the incident and reflected pressure waves exactly cancel each other, i.e., if

$$p'(x, L) = 0, \quad (17)$$

which implies a real reflection coefficient:

$$\tilde{R}_e = -1 \quad (18)$$

6.1.2 Interface/Acoustic Reflection

The arrival of an interface wave to an open end creates a complicated perturbation, the net result of which can only be an upstream propagating acoustic wave, since interface waves can move only downstream. The reflection is an interface/acoustic type and can be characterized by complex reflection coefficients:

$$p'_- = Q_{ep} p'_* \quad (19)$$

$$u' = Q_{eu} p' , \quad (20)$$

where the perturbation quantities on the right sides are those associated with an arriving interface wave.

6.2 Externally Imposed Perturbation

The flowfield behavior in the immediate vicinity of the exciter was complex and of no interest for the purposes of the contract. Furthermore, the specification of a boundary condition as a time-dependent cross-sectional area would introduce unnecessary complications into a theoretical description. These difficulties were bypassed by monitoring the time history of the wall static pressure at an arbitrarily chosen location in the constant-area channel, several duct-heights upstream of the exciter. For the purposes of a theoretical description, the measured pressure history is used as a specification of the net pressure perturbation

$$p'_e(L,t) = F e^{-i\omega t} , \quad (21)$$

where p'_e includes contributions from all three waves:

$$p'_e = p'_+ + p'_- + p'_* , \quad (22)$$

F is the amplitude, and ω is the frequency of the excitation, both considered real. The phase angle at this location is thus specified as zero, and thereby $x = x_e = L$ serves as the reference location for phase angles.

6.3 End of Core Flow

The existence of the interface wave presupposes the existence of a clearly defined interface, i.e., a distinct boundary layer. Boundary layers always exist behind the shock, but their streamwise extent is limited. Under

a strong-shock condition, the top- and bottom-wall boundary layers merge about 6-8 throat-heights downstream of the shock, beginning a transition to a fully developed channel flow. At the merger point, the two interfaces disappear, and the transverse wave motions supported by them are no longer possible. The merging region thus acts as a boundary, accounting for the observation that natural oscillation frequencies scale with the length of the core flow in strong-shock cases⁴ (which are known to be dominated by interface waves).

The merger (and the reflection process) occurs over a finite streamwise extent, and little is known about details. It is reasonable to assume, however, that it generates pressure perturbations that propagate in both directions as acoustic waves. If we consider this process as being local, then it can be modeled as the conversion of an arriving interface wave into two acoustic waves. The corresponding reflection and transmission coefficients to be applied at the merger location are

$$P'_+ = T_c P'_* \quad (23)$$

and

$$P'_- = R_c P'_* \quad (24)$$

Nothing is known about actual values; at present they can at best be considered as adjustable constants, to be varied within reasonable limits to match experimentally determined amplitude and phase-angle distributions.

7. OSCILLATIONS

The elementary waves of Section 4 may combine into various oscillatory patterns, depending primarily on the boundary conditions applied. All patterns must contain the upstream acoustic wave, which is the only one capable of moving in that direction. Since there are two types of downstream waves, the relative magnitude of these is an important basis for classification. We distinguish three cases, depending on the ratio of the interface/acoustic wave amplitudes:

- a) acoustic oscillations, $R \gg Q$, modeled by taking $Q = 0$,
- b) compound oscillations, $R \neq 0$, $Q \neq 0$, and
- c) interface oscillations, $R \ll Q$, modeled by taking $R = 0$.

Case (a) represents classical acoustics, closely describing the weak-shock oscillations in model G and the observations made in Naval Weapons Center investigations (References 16 and 17). In case (c) flows, the downstream propagation is dominated by the interface waves. Case (b) is a intermediate situation in which both acoustic and interface waves participate significantly in downstream propagation. Strong-shock oscillations in MDRL models are described by case (b), although the simpler limiting case (c) might be adequate in some situations.

7.1 Acoustic Oscillations

Classical acoustics¹⁸ and aeroacoustics¹⁹ are disciplines in advanced stages of development, allowing accurate prediction of oscillatory properties, as long as the system conforms to the assumptions implicit in the concepts of linear acoustics. In the following, we discuss theoretical predictions for the simple, constant-area model of Figure 1c.

7.1.1 Energy Considerations

It is possible to define quantities called acoustic energy per unit volume (E) and acoustic intensity per unit area (\vec{I}), such that they obey an integral conservation relation for a fixed volume¹⁹:

$$\frac{\partial}{\partial t} \int E dV = - \oint \vec{I} \cdot d\vec{s} , \quad (25)$$

or, for a one-dimensional situation,

$$\frac{\partial}{\partial t} \int_0^L E S dx = - [IS]_0^L. \quad (26)$$

The integral on the left side represents the energy content of the volume V that is attributable to the presence of acoustic waves, and the right side describes the energy flux carried in and out of the volume by acoustic waves. For one-dimensional flows, E and I are both scalars and are defined as¹⁹

$$E = \frac{\gamma}{2} \bar{p} (P + U)^2 \quad (27)$$

and

$$I = \gamma \bar{p} a (P + \bar{M}U)(U + \bar{M}P), \quad (28)$$

where

$$P = \frac{p'}{\gamma \bar{p}}, \quad U = \frac{u'}{a}. \quad (29)$$

The above definitions apply at any instant in time-dependent flows. For engineering purposes, the time-mean values are of more interest.

In the case of constant-amplitude, periodic oscillations, time-averaging of Equation (26) yields zero on the left side, and the acoustic energy fluxes at the two ends of the region are therefore equal. The time-averaged acoustic energy flux into the system at the shock (i.e., at $x = 0$) can be written as

$$\frac{\bar{I}}{\gamma \bar{p} a} = \frac{1}{2} \left[(1 + \bar{M}^2) \overline{PU} + \bar{M}(\overline{P^2} + \overline{U^2}) \right] = \frac{1}{2} \bar{P}^2 \left[(1 + \bar{M}^2) A_r + \bar{M}(1 + A_r^2) \right], \quad (30)$$

where the second expression states the flux in terms of the real part of the admittance ratio.

Equation (30) permits some interesting conclusions. Setting $\bar{M} = 0$ recovers a result well known from the classical acoustics of stationary media. In this case, the system gains or loses energy according to A_r being positive or negative. If $A_r = 0$, the reflection coefficient is unity (Equation (10), hard-wall end-condition) and the system simply conserves the energy it initially contains.

If $\bar{M} > 0$, the first term inside the bracket still corresponds to gain or loss depending on the sign of A_r , while the second term is always positive and therefore always a gain. The net energy exchange is negative (loss) if the real part of the admittance ratio is within the range:

$$-\frac{1}{\bar{M}} < A_r < -\bar{M}. \quad (31)$$

The net energy flux is zero at both limits and positive outside the A_r range defined by Equation (31).

For idealized reflections from a plane shock (Section 5.1) $A_r \approx -1$, the reflection coefficient is nearly zero, and therefore most of the incident acoustic wave energy is lost through the shock, thereby strongly damping the oscillations. In steady state (forced oscillations), the energy lost through the shock is replaced by an identical gain at the downstream end (at $x = L$).

7.1.2 Solutions of the Acoustic Wave Equations

The flow in the configuration of Figure 1c is described by assuming a one-dimensional, inviscid, isentropic, subsonic flow of a perfect gas at a given, constant mean Mach number. The region of interest is bounded by a plane normal shock at its upstream end ($x = 0$) and will be specified to have reflective properties characterized by a known reflection coefficient R . Assuming that all fluctuating properties vary as $e^{-i\omega t}$, a general solution for pressure perturbations can be obtained in the form (Reference 14)

$$p'(x, t) = \left(\tilde{p}_+ e^{iKx} + \tilde{p}_- e^{-iKx} \right) e^{-i(\omega t + \bar{M}Kx)}, \quad (32)$$

where

$$\tilde{K} = \frac{\tilde{\omega}}{\tilde{a}(1 - \tilde{M}^2)} \quad (33)$$

and \tilde{P}_+ and \tilde{P}_- are complex constants corresponding to downstream and upstream waves. $\tilde{\omega}$ is the oscillation frequency and is, in general, a complex constant. $\tilde{\omega}$ with a nonzero imaginary part describes growing or decaying oscillations, depending on whether ω_i is positive or negative.

Special cases of Equation (32) will be discussed in the next two sections.

7.1.2.1 Natural Oscillations with Open Duct-End

Imposition of the homogeneous conditions discussed in Section 6.1.1 (Equation (17)) results in a homogeneous problem whose solution can be shown to exist only if $\tilde{\omega}$ assumes discrete values, given as

$$\tilde{\omega}_n = \frac{\tilde{a}(1 - \tilde{M}^2)}{2L} \left\{ \left[(2n - 1)\pi - \phi \right] + i [\ln R] \right\}, \quad n = 1, 2, 3, \dots \quad (34)$$

These values are the natural (eigen) frequencies of the system. The imaginary part of $\tilde{\omega}_n$ depends on the absolute value of the reflection coefficient only and describes a decaying or growing oscillation, depending on R being less than or greater than unity. If $R = 1$ the oscillations occur at a stationary amplitude (forced oscillations).

The frequency (real part of $\tilde{\omega}$) is independent of R but depends on the phase angle ϕ . Positive ϕ (phase delay) reduces the natural frequency, the effect being especially strong for low harmonics where ϕ is comparable to $(2n - 1)\pi$.

If \tilde{R} is a specified complex number, Equation (34) unambiguously determines the natural frequency of the system. However, if the upstream boundary condition is to reflect the behavior of a normal shock, then ϕ depends on the frequency in the manner illustrated in Figure 6b. Thus there

exist two relations between the real part of ω_n and ϕ that must be satisfied: Equation (4) and the relation illustrated in Figure 6b. The ω_n values satisfying both relations determine the correct natural frequencies.

The procedure of finding the solution can be illustrated graphically. Using the normalization of ω introduced in Section 5.1, the real part of Equation (34) can be rewritten as

$$\phi_n = (2n - 1)\pi - \left(\frac{2}{1 - \bar{M}^2} \right) \left[\frac{d \ln S}{d(x/L)} \right] \Omega_n . \quad (35)$$

These relations are shown in Figure 6b as dashed lines for $n = 1, 2, 3$. The intersection of the dashed lines with a continuous line for a selected \bar{M} yields the desired frequencies. The results approximate sequences of integer numbers; in the illustrated example the approximate proportions are 1:3.1:5.6. Having determined Ω_n , the magnitude of the reflection coefficient is directly given by Figure 6a.

The frequency dependence of \tilde{R} may be important in practical prediction attempts. In the following, however, we simplify discussions by considering \tilde{R} as a fixed, known quantity.

Having obtained the natural frequencies, it is a simple matter to calculate the streamwise distributions of local amplitudes and phase angles for the pressure perturbations, both of which depend parametrically on \bar{M} , R , ϕ , and n .

The effects of varying R on the second harmonic ($n = 2$) distributions are illustrated in Figure 8 for a typical Mach number of 0.78. The amplitude distributions show that a nodal point exists only if $R = 1$, which is expected since complete cancellation of two wave trains can occur only if they have identical amplitudes. If $R \neq 1$, then a minimum occurs near (but not exactly at) the location of the nodal point in the $R = 1$ case. The phase-angle variations for the $R = 1$ case display an abrupt change of 180° at the nodal point. Between the nodal points, the net perturbations move in the upstream direction, indicated by the negative slope of distributions. The abrupt change at the nodal point (characterizing the $R = 1$ case) becomes an increasingly gradual transition as R tends from unity. If $R < 1$, the

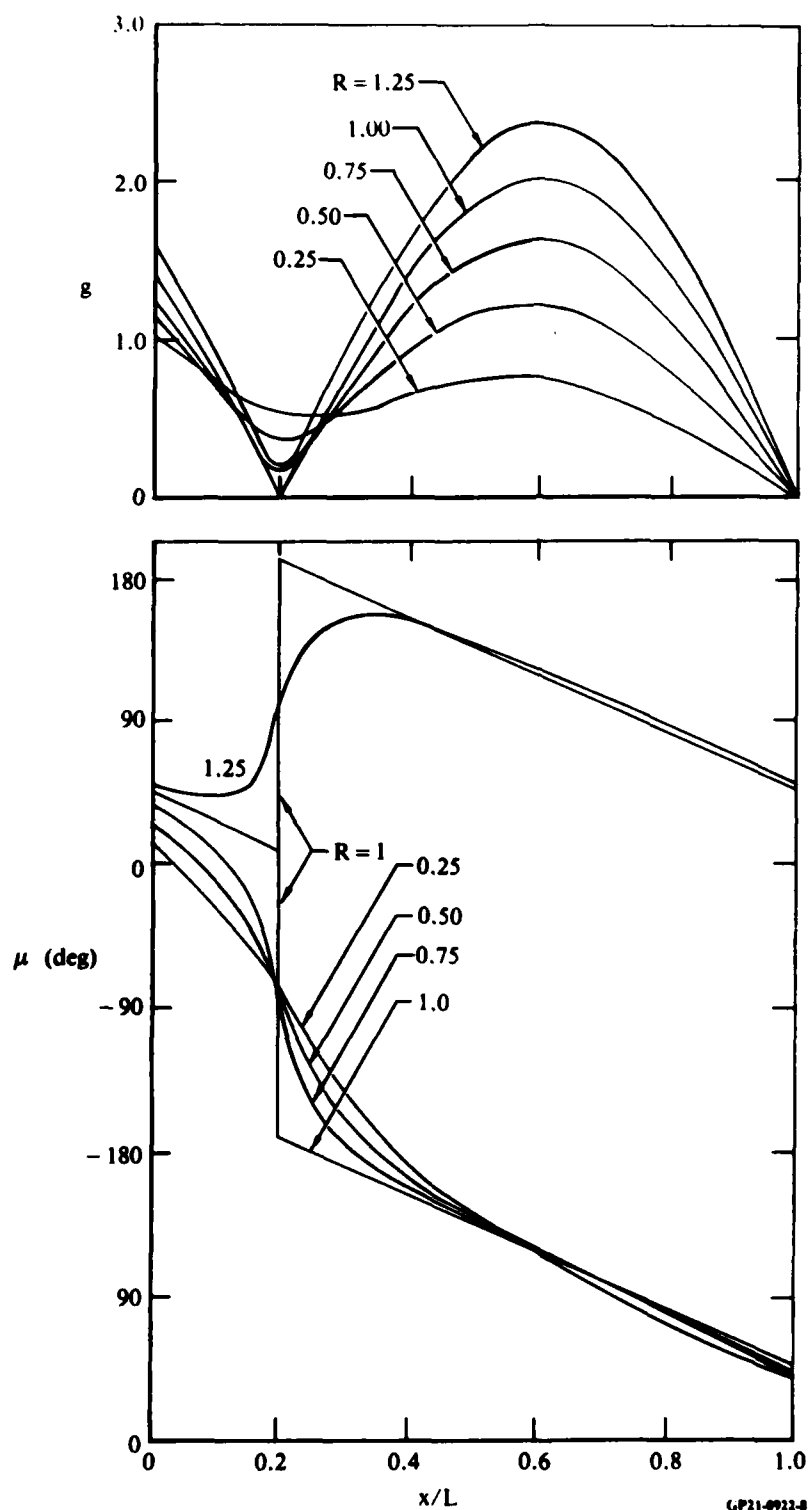


Figure 8. Amplitude and phase angle distribution for an acoustic, natural oscillation, with reflection coefficient magnitude (R) as the parameter. $\bar{M} = 0.78$, $\phi = 90^\circ$, and $n = 2$.

transition is a rapid decrease of g , while for $R > 1$, the change is a rapid increase of g . The latter implies upstream propagation of the net perturbations for a narrow x/L range (from the minimum of the $g(x)$ curve to its maximum).

Figure 9 illustrates how the distributions change as the reflection phase angle (ϕ) is varied. Increasing phase angle causes a smaller multiple of the wavelength to be included in the region, paralleling the reduction of the associated natural frequency (Equation (34)).

7.1.2.2 Forced Oscillations

The imposition of a specified amplitude at the downstream end according to Equation (21) results in an inhomogeneous problem, whose solution describes a stationary oscillation (ω real). The efflux of energy at the shock is non-zero but it is replaced by an equal, steady influx of energy at the driven end. After considerable manipulation, the solution for pressure perturbations is

$$\frac{p'(x, t)}{F} = g(x)e^{-i[\omega t + \hat{g}(x)]}, \quad (36)$$

where $g(x)$ and $\hat{g}(x)$ are real-valued functions defined by the relations

$$g(x) = \left[\frac{1 + R^2 + 2R \cos(2Kx + \phi)}{1 + R^2 + 2R \cos(2KL + \phi)} \right]^{1/2} \quad (37)$$

and

$$\hat{g}(x) = MK(x - L) - \mu(x), \quad (38a)$$

where

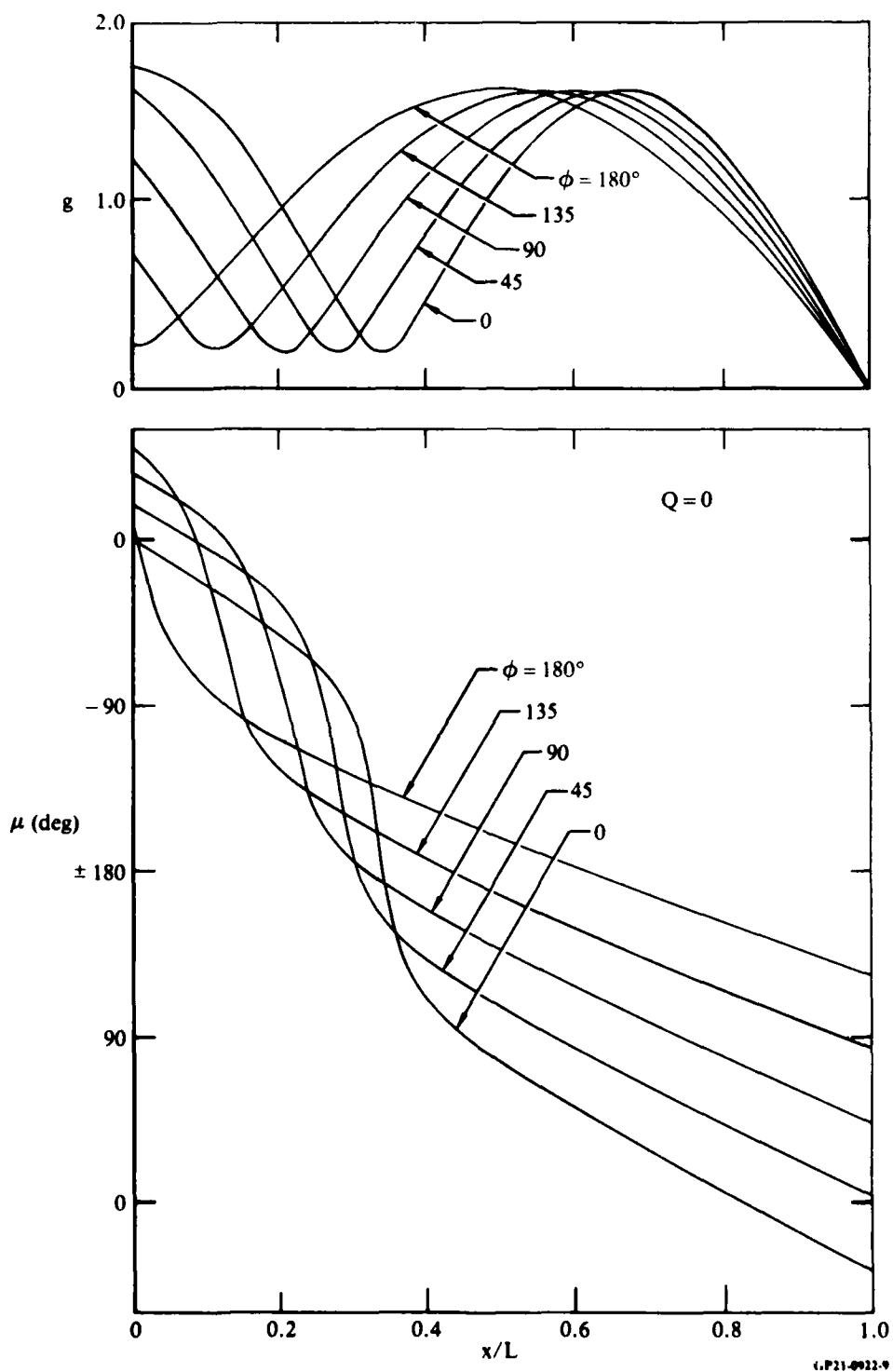


Figure 9. Amplitude and phase angle distributions for an acoustic, natural oscillation, with reflection coefficient argument (ϕ) as the parameter. $\bar{M} = 0.78$, $R = 0.75$, and $n = 2$ (second harmonic).

$$\mu(x) = \sin^{-1} \left[\left(\frac{R^2 - 1}{\sqrt{1 + R^2 + 2R \cos (2KL + \phi)}} \right) \left(\frac{\sin K(x - L)}{\sqrt{1 + R^2 + 2R \cos (2Kx + \phi)}} \right) \right]. \quad (38b)$$

Similar procedures yield the velocity perturbations:

$$\frac{\bar{\rho} \tilde{u}}{F} = h(x) e^{-i[\omega t + \hat{h}(x)]}, \quad (39)$$

where $h(x)$ and $\hat{h}(x)$ are real functions defined as

$$h(x) = \left[\frac{1 + R^2 - 2R \cos (2Kx + \phi)}{1 + R^2 + 2R \cos (2KL + \phi)} \right]^{1/2} \quad (40)$$

and

$$\hat{h}(x) = MK(x - L) - v(x), \quad (40a)$$

where

$$v(x) = \cos^{-1} \left\{ \left[\frac{R^2 - 1}{\sqrt{1 + R^2 + 2R \cos (2KL + \phi)}} \right] \frac{\cos K(x - L)}{\sqrt{1 + R^2 - 2R \cos (2Kx + \phi)}} \right\}. \quad (41b)$$

For the present problem, the absolute value and the argument of the admittance \tilde{A} can be derived as

$$A(x) = \left[\frac{1 + R^2 - 2R \cos (2Kx + \phi)}{1 + R^2 + 2R \cos (2Kx + \phi)} \right]^{1/2} \quad (42)$$

and

$$\tan[A(x)] = \left(\frac{R}{1 - R^2} \right) \sin(2Kx + \phi). \quad (43)$$

These simple analytical expressions permit a clear illustration of reflection effects on forced oscillatory solutions.

(a) $R = 1$. The upstream and downstream waves have equal amplitudes and form a resultant wave traveling upstream at a constant phase velocity of $v = \bar{a}(1 - \bar{M}^2) / \bar{M}$. The local amplitude of the net oscillation changes as a function of x , as determined by the function $g(x)$. Since the two elementary waves are of equal amplitude, a complete, steady cancellation can occur at specific locations (nodal points). If $M \rightarrow 0$, then the phase velocity tends to infinity, corresponding to the standing waves found in classical organ-pipe oscillations. There is no energy transfer between the system and the environment at either end, with or without flow.

(b) $R = 0$. There is no reflected wave originated at the shock, and the pattern consists of a single wave-family, propagating upstream at a phase velocity $v = \bar{a}(1 - \bar{M})$. The amplitude is unchanging; the waves simply pass through the system. There are no nodal points for either velocity or pressure, and there are no standing waves for any value of the Mach number.

(c) $0 < R < 1$. The reflected wave amplitude is less than that of the arriving wave, precluding a total cancellation of the two families. As formally indicated by Equation (37), the amplitude is never zero, and thus there can be no nodal points. The functions $\mu(x)$ and $v(x)$ are not zero, and the phase velocity is a function of x .

Consideration of Equation (37) permits solution of the experimentally important problem of finding the reflection coefficient from a known (experimentally determined) streamwise amplitude distribution. The problem is particularly simple if $g(x)$ has at least two extrema. Designating conditions at the upstream-most minimum and maximum of $g(x)$ by subscripts *min* and *max*, respectively, the following relations can be deduced from Equation (37):

$$R = \frac{g_{\max} - g_{\min}}{g_{\max} + g_{\min}} \quad (44)$$

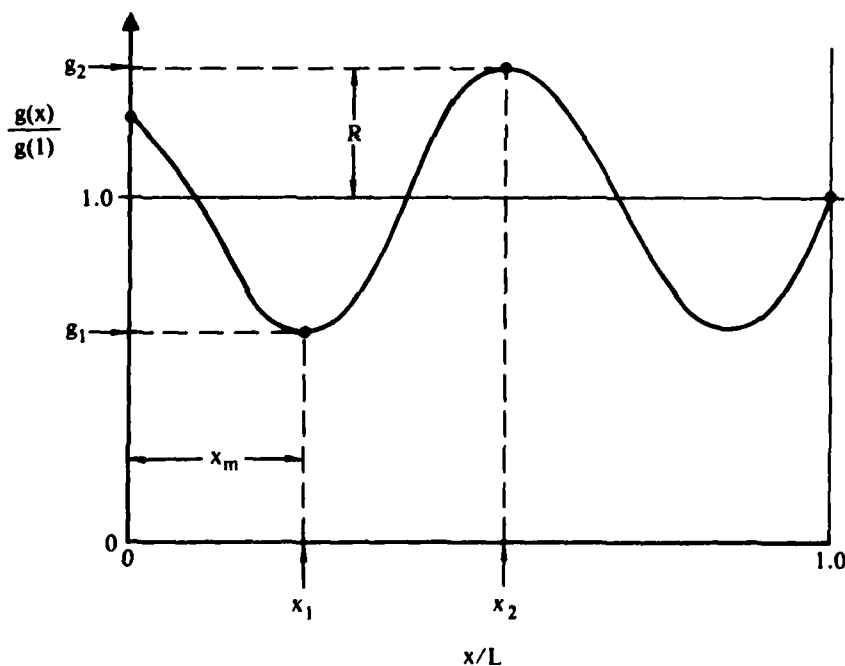
and

$$\frac{\phi}{\pi} = \frac{x_m}{x_{\max} - x_{\min}}, \quad (45)$$

where x_m is the smaller of x_{\max} or x_{\min} . If the first extremum is a minimum, then ϕ is positive and the reflection involves a delay. Figure 10 illustrates how this procedure can be reduced to simple graphic clues concerning the magnitude and argument of the reflection coefficient. The procedure should be used with caution because it presupposes the validity of acoustic theory and streamwise constancy of the cross-sectional area.

7.2 Oscillations Incorporating Interface Waves

Failure of the acoustic theory to account for important features of strong shock oscillations and the experimental evidence of strong interface waves in such oscillations suggests that interface waves be incorporated in



(P21-4922-10)

Figure 10. Amplitude distribution for a forced acoustic oscillation and its relation to the reflection coefficient.

the one-dimensional theoretical description. The present section presents evidence that the inclusion of this mechanism improves agreement with experimental results.

Using the elementary wave description of Section 4 and applying the upstream boundary conditions of Sections 5.1 and 5.2, the pressure perturbation field is written as

$$p'(x, t) = \underline{p} \left[e^{-i\tilde{k}_- x} + \underline{R} e^{i\tilde{k}_+ x} + \underline{Q} e^{i\tilde{k}_* x} \right] e^{-i\omega t}, \quad (46)$$

where the terms in the bracket describe the upstream acoustic, the downstream acoustic, and the interface waves. Also,

$$\tilde{k}_{\pm} = \frac{\omega}{a(1 \pm \bar{M})} \quad (47)$$

and

$$\tilde{k}_* = \frac{\omega}{w} = \frac{\omega}{aW}, \quad (48)$$

where w is the speed of the interface wave in the laboratory frame and W is its value normalized by the speed of sound.

Setting $\underline{Q} = 0$ reduces Equation (46) to the case of classical acoustics, while setting $\underline{R} = 0$ corresponds to the limit of a vanishing downstream acoustic wave. This limiting is termed interface oscillation to distinguish it from the general case involving all three waves, which will be referred to as compound oscillation.

7.2.1 Interface Oscillations

This case, obtained from Equation (46) by setting $\underline{R} = 0$, is formally similar to acoustic oscillations, but quantitative differences in the wave speeds put the solution into a different category. In acoustic oscillations,

the downstream wave is faster than the upstream wave, whereas in interface oscillations, the two are of comparable magnitude.

It is easily shown that the superimposition of two waves of equal amplitude traveling in opposite directions produces a resultant traveling wave that moves in the direction of the component wave with the smaller speed. The resultant wave speed, V , is given by the relation

$$\frac{1}{V} = \frac{1}{2} \left(\frac{1}{u_+} - \frac{1}{u_-} \right). \quad (49)$$

The upstream wave is always acoustic, so that $u_- = a - u$ in both acoustic and interface oscillations. In the acoustic case, $u_+ = a + u$; therefore u_+ is always greater than u_- , and the resultant wave always propagates upstream. For interface waves, $u_+ = w$, which may be either smaller or greater than $a - u$. The condition for downstream propagation thus is

$$\bar{w} < (\bar{a} - \bar{u})$$

or

$$\bar{w} < (1 - \bar{M}) . \quad (50)$$

Equation (50) may well be satisfied; therefore the interface oscillation model has the potential of accounting for the observed downstream propagation of the resultant wave in strong shock oscillations.

If the amplitudes of the two wave-trains are not equal, then the criterion for downstream propagation is more complex; the larger amplitude wave tends to dominate the pattern.

In order to examine natural interface oscillations, we apply the boundary condition of Equation (17) to Equation (46), with $R = 0$.

$$p'(L, t) = \bar{p}_- \left[e^{-ik_- L} + Q e^{ik_+ L} \right] e^{-i\omega t} = 0 . \quad (51)$$

From this equation, the natural frequencies are found as

$$\omega_j = \frac{\bar{a}}{L} \left[\frac{1}{1 - \bar{M}} + \frac{1}{\bar{w}} \right]^{-1} \left\{ \left[(2j - 1)\pi - \psi \right] + i [\ln Q] \right\}, \quad j = 1, 2, 3, \dots \quad (52)$$

The similarities between Equations (52) and (34) (describing acoustic oscillations) are evident. Comparison of Figures 8 and 11 shows that the amplitude distributions are virtually identical in the two cases. The most immediate conclusion of practical importance following from this finding is that interface oscillations cannot be distinguished from acoustic oscillations on the basis of amplitude distributions alone; the streamwise distribution of phase angles must also be considered. Comparison of Figures 8 and 11 shows that (between the nodal points) the phase velocity is negative for acoustic and positive for interface waves. This distinction exists only if $\bar{W} > (1 - \bar{M})$. If the opposite is true, then the phase velocity is negative in both cases. If $\bar{W} = 1 - \bar{M}$, then the phase velocity is infinite ($dg/dx = 0$), standing waves result, and the amplitude and phase distributions agree exactly with classical organ-pipe solutions, obtained assuming a stationary medium.

Even though the amplitude (and for the $\bar{W} < 1 - \bar{M}$ case, even the phase angle) distributions may be identical, the frequencies associated with each case are not; the interface oscillation frequencies are significantly lower than the corresponding acoustic ones.

Equation (52) suggests that the natural frequencies associated with interface oscillations vary inversely with L , in apparent contrast to experiments demonstrating independence of geometric length. The paradox can be resolved by identifying L with the length of the core flow and the open-end reflection with the more complex process occurring in the merging region, as described in Section 6.3. The boundary condition here is presumably different from the simple $p' = 0$ constant condition of Equation (17), but at the present stage of limited understanding, the application of more complex models would be premature. Since the value of ω_{jr} does not depend on Q and its dependence on ϕ becomes increasingly weaker for increasing j , the natural frequencies given in Equation (52) are probably reasonable despite uncertainties in the value of Q .

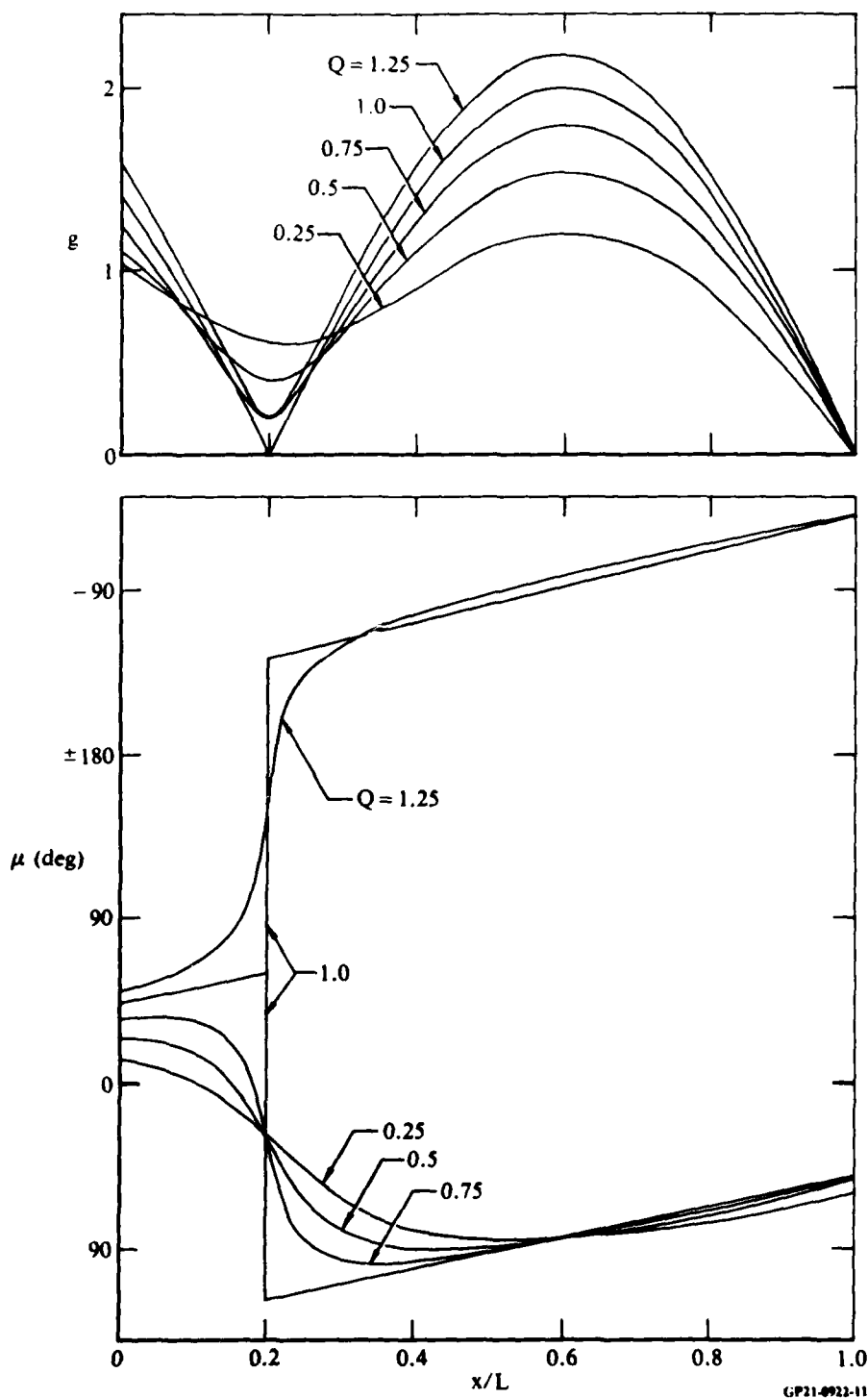


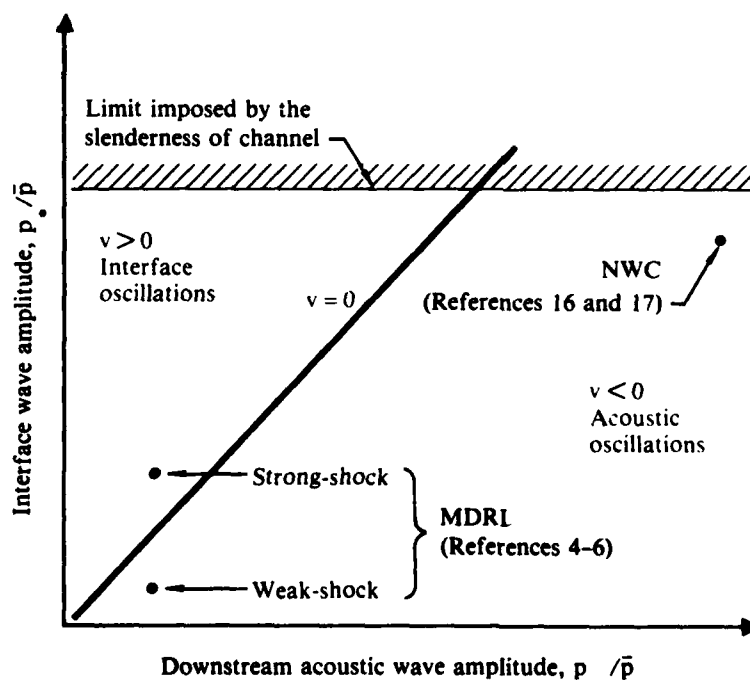
Figure 11. Amplitude and phase angle distributions for a natural interface oscillation, with reflection coefficient magnitude (Q) as the parameter. $\bar{M} = 0.78$, $\bar{W} = 0.1$, $\psi = 90^\circ$, and $j = 2$ (second harmonic).

7.2.2 Compound Oscillations

Compound oscillations are, by definition, those appreciably affected by both interface and downstream acoustic waves. Depending on the relative amplitude of the two competing downstream waves, different types of oscillations may result.

For small amplitudes, the ratio of P_{*}/P_{+} is controlled by the ratio of reflection coefficients Q/R . For large amplitudes, this dependence may not be the case because the acoustic wave amplitude may be made large by applying large amplitude excitation, whereas the interface wave amplitude must remain below the inherent limit discussed in Section 4.2.

Figure 12 illustrates how apparent contradictions in three known relevant experiments can be resolved in terms of compound oscillations. The figure shows regions of positive and negative v (downstream- and upstream-moving resultant waves). The axes correspond to the acoustic and interface limits.



GP21-0922-12

Figure 12. Regions of compound oscillations and their relation to three experimental observations. Scales are arbitrary.

MDRL experiments⁵ always involved small-amplitude perturbations, and the interface wave strength was controlled by Q ; the result is an upstream-moving net wave for weak shocks and downstream net wave for strong ones.

The third case shown describes investigations at Naval Weapons Center (NWC)^{16,17} of large-amplitude oscillations in a direct-connect ramjet experiment. The oscillations appear to follow acoustic predictions, in conflict with MDRL results since the terminal shock was strong ($M_0 \sim 1.5$) and its oscillations would be expected to generate significant interface waves. In the NWC experiment, the oscillations were driven by a large-amplitude combustion instability ($\pm 20\%$), which set a high level for the longitudinal waves, apparently well over the maximum possible amplitude for the interface waves. The dominant elements of the oscillations were thus the two acoustic wave-families, and the wave resulting from them naturally follows acoustic predictions.

The natural frequencies for compound oscillations in our idealized model (Figure 1c) are determined by applying the boundary condition of Equation (17) to Equation (46):

$$p'(L, t) = \underline{p}_- \left[e^{-ik_-L} + \underline{R}e^{ik_+L} + \underline{Q}e^{ik_*L} \right] e^{-i\omega t} = 0. \quad (53)$$

The roots of this equation (obtained by numerical procedures) form a sequence of complex numbers, labeled by the subscript $k = 1, 2, 3, \dots$, in the order of increasing magnitude of their real parts. As illustrated in Figure 13, compound natural oscillations are possible at more frequencies than the number of natural modes for acoustic oscillations. For $0 < Q < 2$, there are only two acoustic frequencies for the illustrated case, but no less than five compound natural frequencies were found. If Q is decreased towards zero, then the $k = 1$ mode approaches the lowest ($n = 1$) acoustic mode, while the $k = 4$ mode becomes the second ($n = 2$) acoustic mode. The $k = 2$ and 3 compound modes have no equivalent acoustic patterns, although the $k = 2$ case comes close to the fundamental acoustic mode in the $Q \rightarrow 0$ limit.

Each complex root (natural frequency) is associated with a particular spatial distribution of amplitudes and phase angles. Figure 14 illustrates a family of such distributions for $k = 2$, with Q as a parameter proportional to

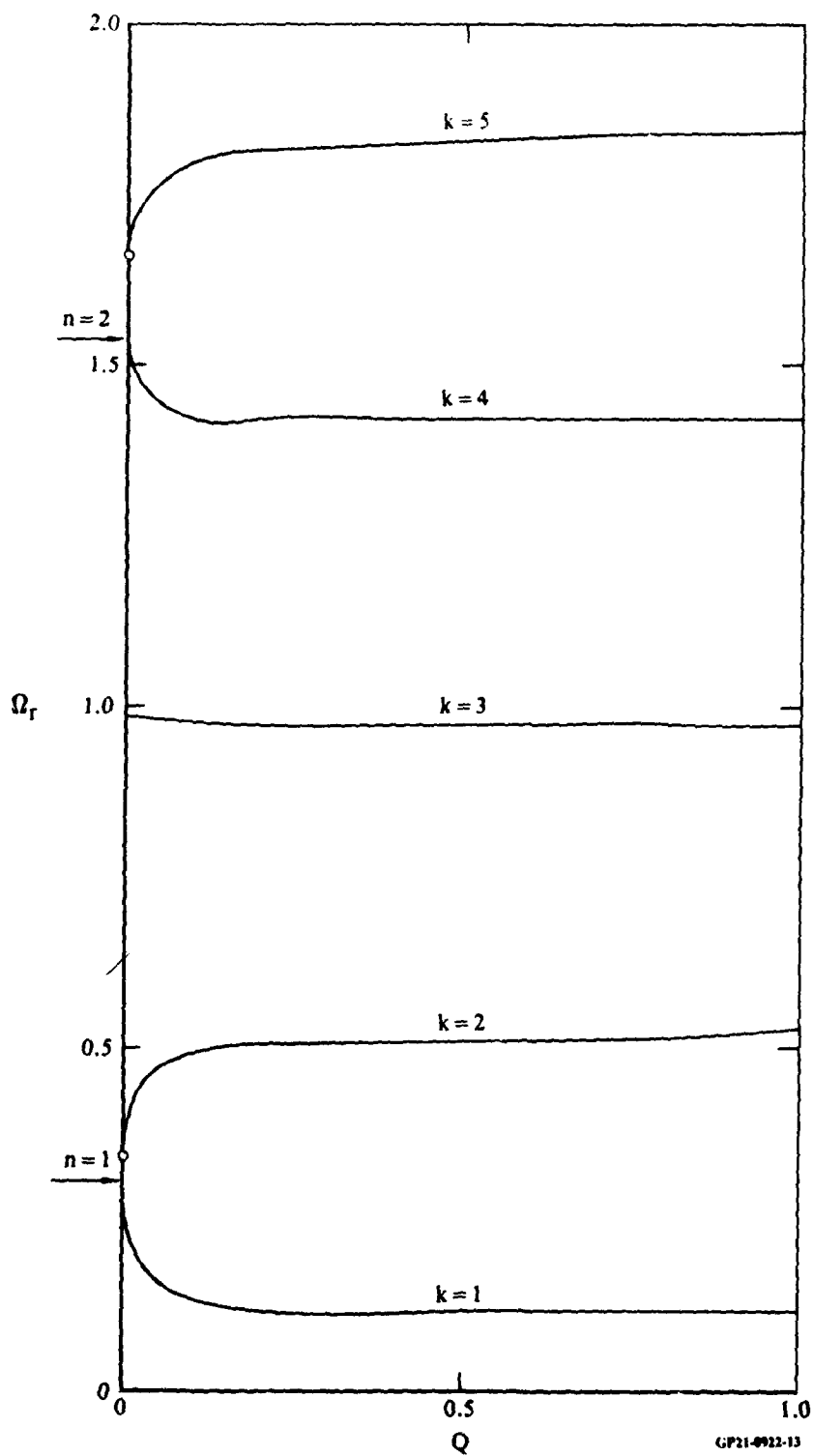


Figure 13. Natural frequencies for compound oscillations ($k = 1$ to 5) and their relation to acoustic natural frequencies ($n = 1, 2$). $\bar{M} = 0.78$, $\bar{W} = 0.1$, $R = 0.25$, $\phi = 90^\circ$, and $\psi = 90^\circ$.

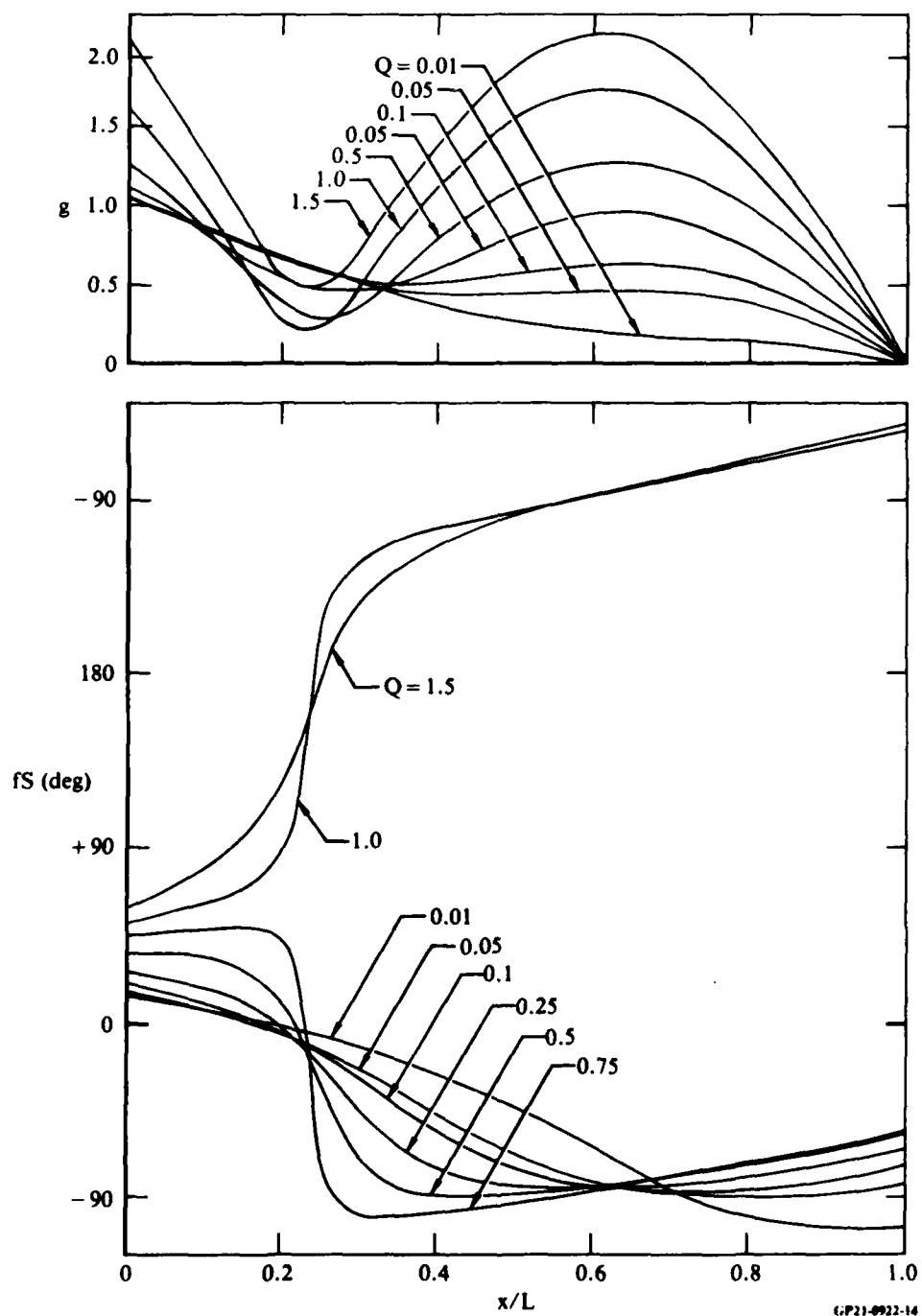


Figure 14. Amplitude and phase angle distributions for compound natural oscillations, with Q as the parameter. $\bar{M} = 0.78$, $\bar{W} = 0.1$, $R = 0.25$, $\phi = 90^\circ$, $\psi = 90^\circ$, and $k = 2$ (second compound mode).

the interface wave contribution. Comparison of Figures 8 and 13 indicates that the $Q \rightarrow 0$ limit does not reproduce the $n = 2$ acoustic oscillation mode.

Figure 15 shows a comparison of measured pressure amplitude and phase distributions with theoretical results for natural acoustic and natural interface oscillations. \bar{M} , \bar{W} , and the reflection coefficients were chosen to maximize agreement with the data. The amplitude distributions are close in both cases, but the phase-angle distributions predicted by acoustic theory bear no resemblance to the data. Furthermore, the frequency of the acoustic oscillations (second harmonic) is 47% higher than the frequency at which the data were taken. In contrast, the compound prediction displays a qualitatively correct phase-angle distribution and frequency within 6% of the experimental case.

This comparison is highly qualitative for several reasons: the theory is for a constant-area channel exhibiting natural oscillation, while the experimental model had variable area and the data apply to a forced oscillation. The comparison nevertheless shows that by including the physically observed interface wave mechanism, it is possible to predict amplitude and phase distributions that are qualitatively in agreement with experimental results, using physically reasonable choices for the unknown parameters built into the formulation.

In its present form, the one-dimensional, constant-area formulation is a convenient and precise way of stating arguments in favor of a theoretical model. Further work needs to be done by extending the model to variable-area channels, justifying the one-dimensional approach in view of the inherent two- or three-dimensional structure of the pressure and velocity field, and including calculation of the velocity perturbations, in which transverse variations are more prevalent than in pressure perturbations. Finally, experimental information concerning the values of reflection coefficients is needed.

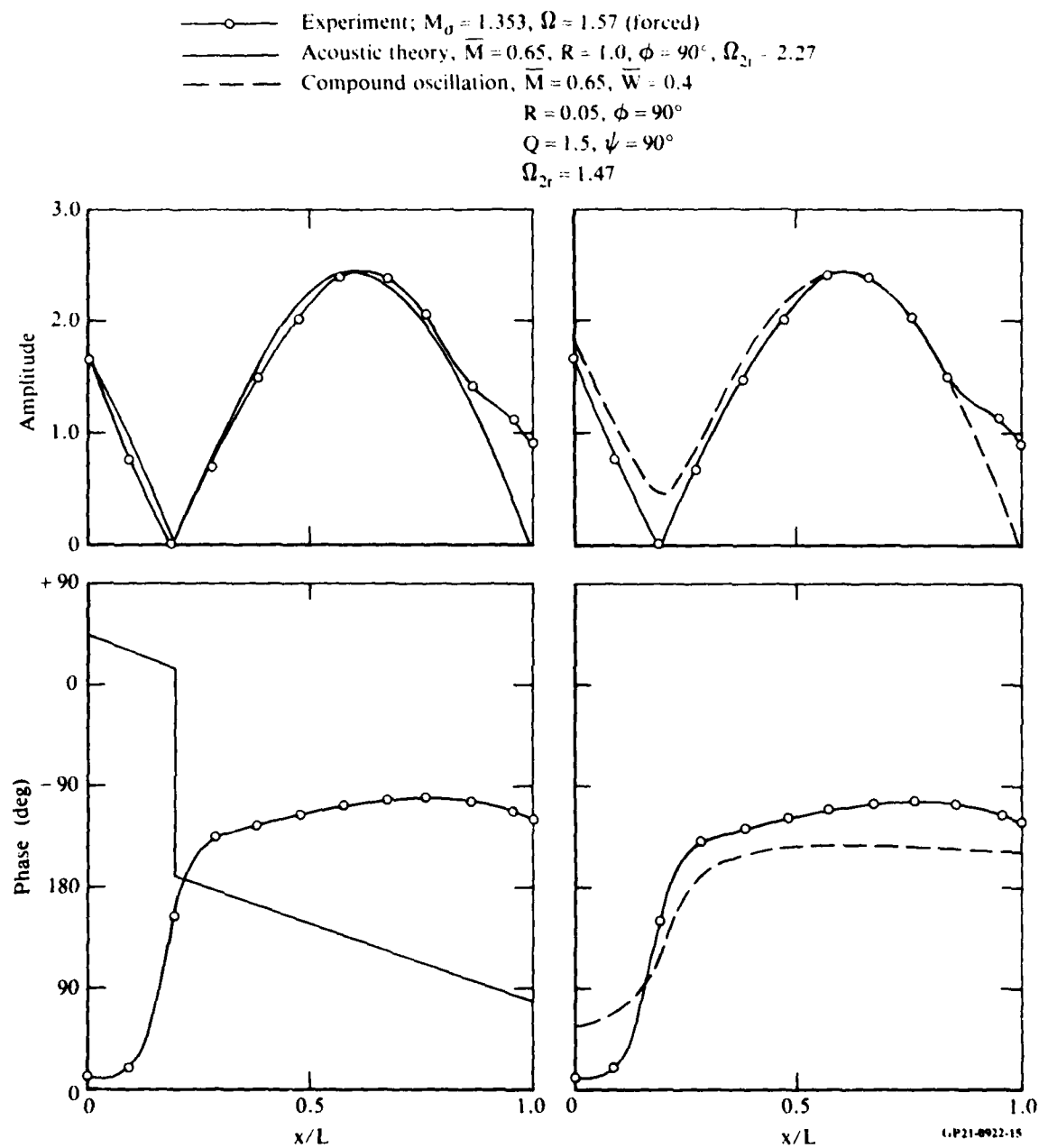


Figure 15. Steamwise distributions of amplitude and phase angle for the second harmonics of the fluctuations of midstream static pressure. Experimental data from Reference 5, Model G, $M_0 = 1.353$, and excitation at 300 Hz.

8. RESONANCE

Extreme values of shock displacement or pressure fluctuation amplitudes in inlet diffusers are of direct engineering concern for obvious operational and structural reasons. Large amplitudes were expected to occur in these experiments when the excitation frequency was equal to any of the natural frequencies. However, no conspicuously large pressure or shock displacement amplitudes were found under such circumstances (Reference 5), which prompted investigations into possible causes.

The definition of the problem at the outset of the inquiry was to determine the conditions necessary for resonance and to determine if resonance occurred in the present experiments. This problem formulation raised conceptual questions as to what constitutes a resonance. No generally applicable, satisfactory answers were found to these questions.

Progress was made, however, by attacking the data interpretation issue from a different point of view. The phenomenon of principal engineering interest is the occurrence of extreme oscillation amplitudes for certain flow properties. Resonance is of interest because it is an important (but not the only) mechanism capable of creating such situations. Vice versa, maximum amplitudes are not necessarily associated with resonance, e.g., overdamped systems may display maximum response in the limit of zero excitation frequency. It is concluded that a less general but more useful definition of the problem is to investigate conditions leading to maximum amplitudes of selected system properties.

In the following, we first discuss resonance in terms of a simple mathematical model and then compare the findings with a real system (for which a mathematical model may not exist).

8.1 Resonance in a Mathematical Model

We consider the constant-area, inviscid, linearized acoustic model described in Section 7.1. The system is a one-dimensional continuum, and its state at any instant is described by distributions of amplitudes and phase angles, not by a single variable such as a simple linear oscillator (e.g., a

spring-mass system). As indicated by Equation (34), the natural oscillation frequencies are complex, including an imaginary part that describes the rate of amplitude decay if $R < 1$ and the system is left undisturbed. The decay is caused by energy lost from the system through the upstream boundary which is a source of localized damping. (Real systems may involve loss mechanisms distributed throughout the system such as turbulent dissipation; these are not represented in our simple model.) The natural frequencies form a one-parameter family and therefore a single set of modes since only longitudinal perturbations are allowed.

The system can be forced to execute steady-state oscillations by prescribing the pressure amplitude at its downstream end. This excitation, which is one of many possible methods, results in the oscillatory patterns described in Section 7.1.2.2. The pattern is described by Equation (36), rewritten here as

$$\frac{p'(x, t)}{E} = C_1 \left[1 + R^2 + 2R \cos (2Kx + \phi) \right]^{1/2} e^{-i[\omega t - \hat{g}(x)]}, \quad (54)$$

where C_1 is a constant coefficient given as

$$C_1 = \left[1 + R^2 + 2R \cos (2KL + \phi) \right]^{-1/2}, \quad (55)$$

where

$$K = \frac{\omega}{\bar{a}(1 - \bar{M}^2)}. \quad (56)$$

Both ω and K are real. The customary interpretation of resonance is that resonance occurs when C_1 has a maximum. It follows from Equation (55) that C_1 has a maximum if the frequency assumes the following (real) values:

$$\omega_n = \frac{\bar{a}(1 - \bar{M}^2)}{2L} \left[(2n - 1)\pi - \phi \right], \quad n = 1, 2, 3, \dots \quad (57)$$

Comparison with Equation (34) indicates that resonance occurs if the excitation frequency is equal to (the real part of) any one of the natural frequencies. The spatial distributions of amplitudes and phase angles in the natural and forced oscillations are similar, but not identical, since $p'(L)$ is zero in the natural mode and finite in the forced mode.

It follows from Equations (55) and (57) that in resonance $C_1 = 1/(1 - R)$ and the maximum normalized pressure amplitude in the system is $(1 + R)/(1 - R)$. If $R = 1$, the system is loss-free and the amplitudes tend to infinity, indicating that the steady net inflow of energy at the downstream end is not compatible with a steady-state oscillation.

This calculation is straightforward. However, consider the problem of a hypothetical experimenter who deals with this ideal system and wants to determine the resonant frequencies. He does not know R and ϕ , but can set excitation frequency and measure pressure amplitude and phase at a finite number of locations from $x = 0$ to L .

Figure 16 (based on Equation (54)) illustrates how the measured local pressure amplitude would vary, should five sensors be located at $0.25 L$ intervals. Frequencies are normalized by the first natural frequency. The problem is apparent: sensors located at different locations indicate peak amplitudes at different frequencies. The amplitude distribution changes constantly as the excitation frequency is varied; the peaks of the distribution shift and change magnitude concurrently, and a fixed sensor detects the net result of both types of changes. The reliable detection of resonance thus requires, even in this simple system, knowledge of the entire pressure distribution with good spatial resolution and for densely spaced frequency values over the frequency range of interest. The acquisition of such an extensive data set may be beyond economic feasibility even for a research-oriented experimentalist, and almost certainly for an engineer doing development work.

8.2 Resonance in a Real System

The supercritical diffuser flows investigated in this project include many complexities not represented in the simple model of the previous sections: some of the more important are briefly discussed.

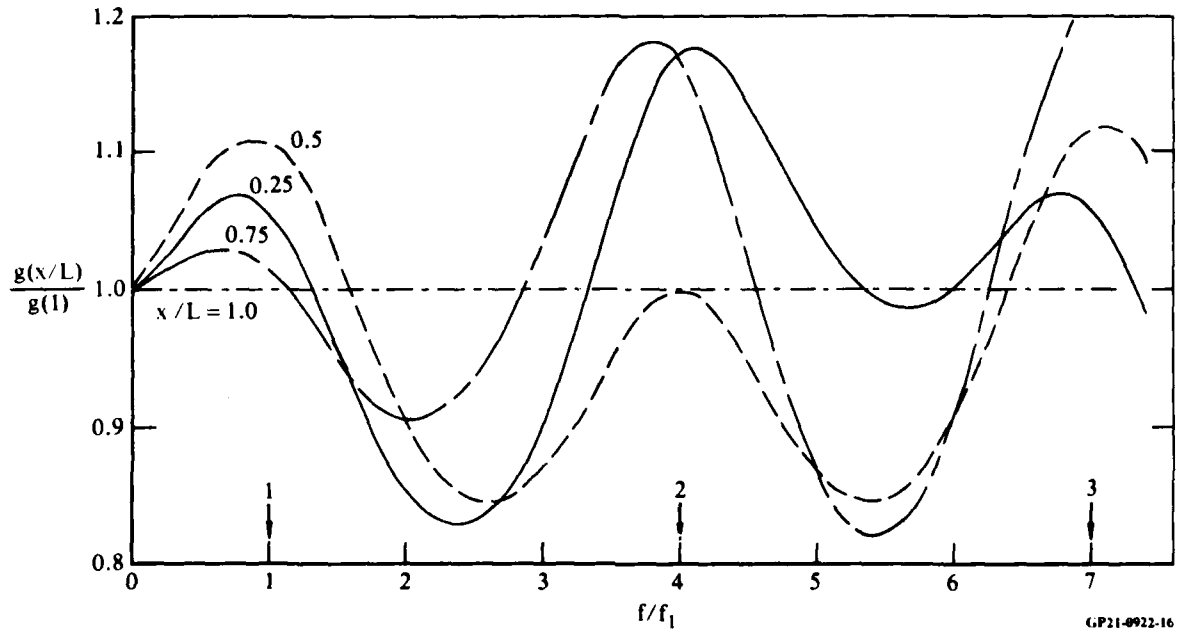


Figure 16. Acoustic oscillation amplitudes detected at various locations in a constant-area channel as functions of excitation frequency. f_1 is the fundamental frequency for open downstream end, $R=0.1$ and $\phi=60^\circ$. Arrows indicate natural frequencies.

The flowfield is two-dimensional and even if it were uniform and inviscid, it could possess two sets of natural modes with appropriate natural frequencies. The excitation technique applied may excite motions belonging to one family, while natural oscillation modes might belong to another. Excitation of a damped mode could explain the apparent absence of resonance, even though the system may be capable of responding with high amplitudes to a different type of excitation.

The flow is significantly nonuniform in both the streamwise and transverse directions and contains regions of intense time-mean dissipation. It is not clear if these regions also strongly attenuate acoustic waves, but they are likely to do so. The effects might be the broadening and reduction of resonant peaks.

Perhaps the most important aspect of dealing with real flows is that there is no manageably simple theoretical model available upon which to base a search for resonance phenomena. Mechanisms other than simple acoustic-wave propagation clearly play an important role, and some of them (convection and

turbulent diffusion) tend to obscure the more sharply defined patterns created by wave motions.

Experimental difficulties and economic limitations further aggravated the situation. The excitation amplitude and frequency varied concurrently (Reference 5), and the effects attributable to each could not be separated. The spatial resolution was insufficient, and the statistical processing necessitated by the low signal-to-noise ratio further reduced the number of cases that could be investigated.

The conclusion is that the resonance issue, in its originally posed, broad form, could not be resolved for both conceptual and practical reasons.

8.3 Extreme Amplitudes

The resonance question proved unmanageably broad, and perhaps also not necessary. For most practical purposes, it may be satisfactory to know the conditions that lead to extreme values of some selected system property.

One such obvious property is the shock oscillation amplitude. For small amplitudes, the shock responds linearly to the pressure oscillation amplitude immediately behind the shock (Section 5.1). For the simple model of Section 7.1, the largest shock oscillation amplitudes occur when p' at $x = 0$ is maximum. Equation (37), with $x = 0$, supplies the amplitude at the upstream end as

$$g(0) = \left[\frac{1 + R^2 + 2R \cos \phi}{1 + R^2 + 2R \cos (2KL + \phi)} \right]^{1/2}. \quad (58)$$

For a given R , the shock motion amplitude is maximum at resonance (which is clearly defined for this model, see Equation (57)). At resonance,

$$[g(0)]_{\max} = \frac{\sqrt{1 + R^2 + 2R \cos \phi}}{1 - R}, \quad (59)$$

which shows that the shock amplitude increases indefinitely as $R \rightarrow 1$ and that the $\phi = 0$ (closed-end like) reflection produces the largest amplitudes.

If attention is focused on a single system property (as opposed to variation of entire distributions), determination of a maximum of this selected property as a function of system parameters is a well-defined, feasible task, even in a real system.

It is important to associate the results with appropriate dimensionless parameters. The experience of this project clearly indicates that the pre-shock Mach number (\bar{M}_σ) is the most significant independent variable, preferable to conventionally used overall pressure ratios. \bar{M}_σ has a decisive influence on development of the post-shock boundary layer and the reflective properties of the shock (Appendix A), thereby controlling major elements entering into the determination of the oscillatory flow.

Inviscid, linearized theory suggests the following normalization of the shock-displacement:

$$X_\sigma = \frac{\bar{p}_2}{p_2} \cdot \frac{d \ln S}{dx} x'_j . \quad (60)$$

Presentation of experimental data in this form shows no simplification of the results in comparison to a straightforward dimensional plot. One possible improvement might be to base normalization on the effective (geometric minus displacement) area. Since shock oscillation effectively prevented determination of boundary-layer properties in the immediate vicinity of the shock, this type of normalization was not possible.

References 2 through 6 contain extensive information which include various extreme values. These values form valid information whether or not their occurrence coincides with a resonance condition.

9. SUMMARY AND CONCLUSIONS

Detailed investigations of data obtained in both natural and forced diffuser flow oscillations indicate that unsteady boundary-layer effects appear in the form of downstream-moving transverse waves carried by the boundary-layer/core-flow interface. These waves, called interface waves, become more intense as the terminal shock strength increases and may dominate over downstream-moving acoustic waves when shock-induced separation is present in the flow.

Preliminary calculations indicate that a quasi-one-dimensional description of these waves may be possible on the same level of complexity as conventional, one-dimensional acoustic calculations. Incorporation of the interface waves accounts for important observations, including the downstream-directed motion of the wave resulting from superposition of the upstream acoustic and the interface waves.

The success of such a theory depends on availability of information concerning the reflection of acoustic and interface waves from the shock and from an open-end duct and the behavior of the interface wave at the location where boundary layers on opposite walls merge. Investigation of these processes is required for further progress towards characterization of supercritical oscillations.

The present study dealt with an intentionally simple system to illustrate major features of the proposed modeling assumption. A calculation method aimed at a quantitative prediction capability will have to include a stream-wise area variation and appropriate modeling assumptions for the prediction of velocity perturbations in the presence of interface waves.

REFERENCES

1. M. Sajben, T. J. Bogar, and J. C. Kroutil, Unsteady Transonic Flows in a Two-Dimensional Diffuser, Final Report MDC Q0767, AFOSR Contract F49620-77-C-0082 (March 1982).
2. M. Sajben and J. C. Kroutil, Effects of Approach Boundary Layer Thickness on Oscillating Transonic Diffuser Flows Including a Shock, AIAA Paper No. 80-0347 (1980).
3. M. Sajben and J. C. Kroutil, Effects of Initial Boundary Layer Thickness on Transonic Diffuser Flows, AIAA J. 17, 1386 (1981).
4. T. J. Bogar, M. Sajben, and J. C. Kroutil, Characteristic Frequency and Length Scales in Transonic Diffuser Flow Oscillations, AIAA Paper No. 81-1291 (1981).
5. M. Sajben, T. J. Bogar, and J. C. Kroutil, Forced Oscillation Experiments in Supercritical Diffuser Flows with Application to Ramjet Instabilities, AIAA Paper No. 81-1487 (1981).
6. M. Sajben, T. J. Bogar, J. C. Kroutil, and J. T. Salmon, Factors Influencing Velocity Distributions at Inlet/Combustor Interfaces, 18th JANNAF Combustion Meeting, Pasadena, CA, CPIA Publication No. 343, Vol. III (1981).
7. T. J. Coakley and M. Y. Bergmann, Effects of Turbulence Model Selection on the Prediction of Aerodynamic Flows, AIAA Paper No. 79-0070 (1979).
8. M.-S. Liou and T. J. Coakley, Numerical Simulations of Unsteady Transonic Flow in Diffusers, AIAA Paper No. 82-1000 (1982).
9. D. D. Knight, Improved Calculation of High Speed Inlet Flows: Part I. Numerical Algorithm, AIAA J. 19, 34 (1981); Part II. Results, AIAA J. 19, 172 (1981).
10. R. W. Newsome, Numerical Simulation of Near-Critical and Unsteady Subcritical Inlet Flow Fields, AIAA Paper No. 83-0175 (1983).
11. J. T. Salmon, T. J. Bogar, and M. Sajben, Laser Velocimeter Measurements in Unsteady, Separated, Transonic Diffuser Flows, AIAA Paper No. 81-1197 (1981).
12. C. P. Chen, M. Sajben, and J. C. Kroutil, Shock-Wave Oscillations in a Transonic Diffuser Flow, AIAA J. 17, 1076 (1979).

13. D. Jacob, On Some Aspects of Shock Wave Oscillations in Supersonic Diffusers. Ph.D. Thesis, University of Tennessee Space Institute, 1968; a summary is given in AFFDL-TR-69-103.
14. F. E. C. Culick and T. Rogers, The Response of Normal Shocks in Inlet Diffusers, AIAA Paper No. 81-1431 (1981).
15. H. G. Hurrell, Analysis of Shock Motion in Ducts During Disturbances in Downstream Pressure, NACA TN 4090 (1957).
16. K. C. Schadow, J. E. Crump, and F. S. Blomschield, Combustion Instability in a Research Dump-Combustor: Inlet Shock Oscillations, CPIA Publication No. 343, III, p. 341 (1981).
17. J. E. Crump, K. C. Schadow, F. S. Blomschield, and C. J. Bicker, Combustion Instability in a Research Dump-Combustor: Pressure Oscillations, CPIA Publication No. 343, III, p. 347 (1981).
18. P. M. Morse and K. V. Ingard, Theoretical Acoustics, (McGraw-Hill Book Co., New York, 1968).
19. M. E. Goldstein, Aeroacoustics, (McGraw-Hill International Book Co., New York, 1976).

APPENDIX A: PRESSURE PERTURBATIONS IN INTERFACE WAVES

Consider Figure A-1, showing a constant-area duct with a displacement wave on the bottom wall (the top-wall boundary layer is omitted for simplicity). Assume that the boundary-layer/core-flow interface locations is given by

$$\delta(x) = \bar{\delta} + \delta', \quad (A-1)$$

where

$$\delta' = \epsilon \cos (\kappa x - \omega t) \quad (\text{A-2})$$

and

$$\pi = \frac{1}{2} \left(\frac{1}{\epsilon_1} + \frac{1}{\epsilon_2} \right) \quad (A-3)$$

The core-flow cross-sectional-area per unit-width of channel is then

$$S_c = S_g - \delta = S_g - (\bar{\delta} + \delta') = \bar{S}_c - \delta' = \bar{S}_c + S'_c \quad (A-4)$$

from which follows

$$S'_c = -\delta'. \quad (A-5)$$

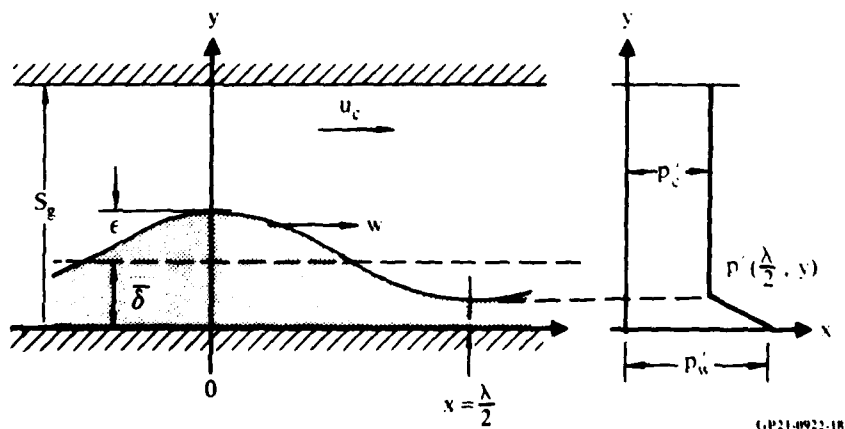


Figure A-1. Interface wave structure.

The phase relation between static pressure and velocity perturbation is easily deduced by considering the flow in a coordinate system moving with the wave, i.e., in the downstream direction, with velocity \bar{w} . In this frame, the shape of the interface is constant in time, and an observer would see a steady flow in a variable-area duct with a (spatial) average velocity of $(\bar{u}_c - \bar{w})$.

Use isentropic relations (in a linearized form) to estimate the pressure variations:

$$\frac{p'_c}{\bar{p}_c} = \frac{\gamma \bar{M}^{-2}}{1 - \bar{M}^2} \frac{s'}{\bar{s}}, \quad (\text{A-6})$$

where \bar{M} is the Mach number seen in the moving frame:

$$\bar{M} = \frac{\bar{u}_c - \bar{w}}{\bar{a}} = \bar{M} - \bar{W}. \quad (\text{A-7})$$

Using Equations (A-4), (A-5), and (A-7), Equation (A-6) becomes

$$\frac{p'_c}{\bar{p}_c} = - \left[\frac{\gamma (\bar{M} - \bar{W})^2}{1 - (\bar{M} - \bar{W})^2} \right] \frac{\delta'}{\bar{s}_c}. \quad (\text{A-8})$$

Equation (A-8) shows that the core pressure perturbation pattern is frozen in the frame moving with the wave. A stationary sensor located in the core flow will detect the passage of this pattern past a fixed point. Equation (A-8) also shows that a maximum of p'_c occurs where δ' has a minimum: the two quantities are 180° out of phase.

For isentropic, adiabatic, steady flows the following general relation is known to hold:

$$dp = - \rho u \, du, \quad (\text{A-9})$$

which can be specialized for the steady flow in our moving frame as

$$p'_c = - \bar{\rho}_c (\bar{u}_c - \bar{w}) u'_c. \quad (\text{A-10})$$

Equation (A-10) indicates that the core flow pressure and core flow velocity are out of phase by 180° , in agreement with experiments.⁵

Equation (A-10) can be used to define a quantity A_* , in analogy to acoustic admittance, as follows:

$$A_* = \frac{\bar{\rho}_c \bar{a}_c u'_c}{p'_c} = - \frac{1}{\bar{M} - \bar{W}} . \quad (A-11)$$

A_* is thus independent of x , in agreement with data and in conflict with acoustic theory (Equations (42) and (43)). Measurements of u' and p' show A_* to be near 1, which compares with values of 1-2 obtained by substituting approximate, average values of \bar{M} and \bar{W} in the right side of Equation (A-11).

The pressure sensed by a fixed, wall-mounted probe differs from the core pressure because of streamline curvature effects (see Figure A-1). In order to estimate this pressure differential, we use the following simple form of the y -momentum equation:

$$\frac{\partial p}{\partial y} = - \frac{\rho u^2}{r} , \quad (A-12)$$

where r is the local radius of curvature of the streamlines. We assume the following transverse variations (with x held constant) for the three quantities appearing on the right side:

$$\rho = \rho_c = \text{independent of } y, \quad (A-13)$$

$$u \begin{cases} = u_c f(y/\delta) & \text{for } y < \delta \\ = u_c & \text{for } y > \delta \end{cases} , \quad (A-14)$$

and

$$\frac{1}{r} = \frac{1}{r_c} h(y/\delta), \quad (A-15)$$

where f and h are appropriate functions left temporarily unspecified.

The radius of curvature for the boundary-layer edge, r_c , is calculated from Equation (A-2):

$$\frac{1}{r_c} = \frac{d^2 \delta'}{dx^2} = -\kappa^2 \delta' . \quad (A-16)$$

Substituting Equations (A-13) to (A-16) into (A-12) and integrating from $y = 0$ to $y = \delta$ results in

$$\frac{p'_c - p'_w}{\bar{p}_c} = \gamma \bar{M}_c^2 I \kappa^2 \bar{\delta} \delta' , \quad (A-17)$$

where I is a definite integral given as

$$I = \int_0^1 f(\eta)h(\eta)d\eta . \quad (A-18)$$

The value of I depends on the velocity and curvature distributions assumed. Reasonable assumptions yield $I = 0.2-0.5$, but the exact value is not too important for the present purposes.

Equation (A-17) is an estimate of the pressure differential caused by streamline curvatures, while Equation (A-8) gives the pressure change caused by streamwise core area variations. Combining two equations gives the net pressure fluctuation detectable by wall-mounted transducers:

$$\frac{p'_w}{\bar{p}_c} = - \left[\frac{\gamma(\bar{M} - \bar{W})^2}{1 - (\bar{M} - \bar{W})^2} + \gamma \bar{M}^2 I \kappa^2 \bar{\delta} \delta' \right] \left(\frac{\delta'}{\bar{\delta}} \right) . \quad (A-19)$$

The two contributions inside the bracket are of the same order of magnitude. These contributions are also in-phase; thus, the wall pressure

fluctuation magnitudes are greater than core pressure amplitudes, as also observed experimentally.

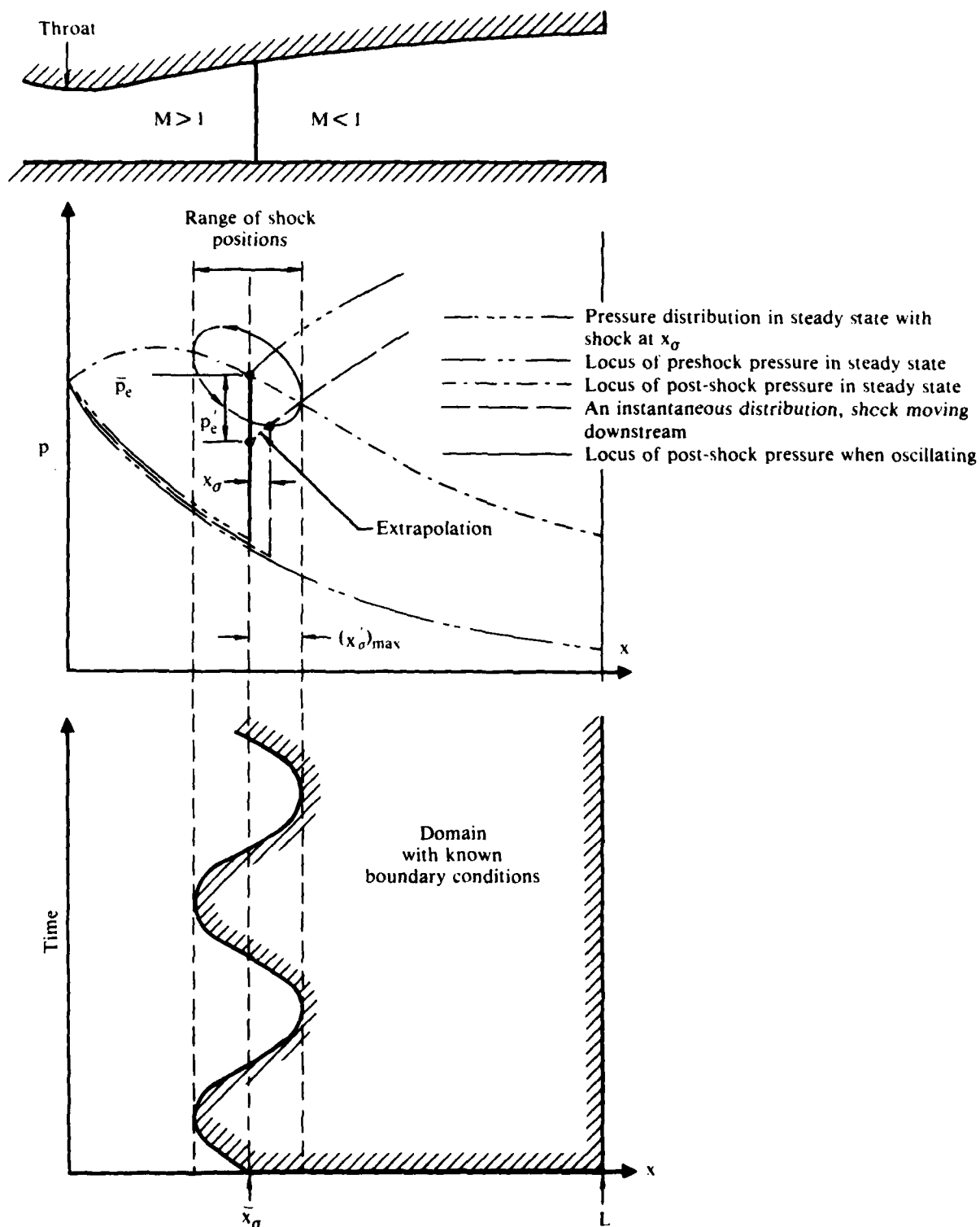
The estimates presented here relate pressure perturbations to boundary-layer displacement effects. The results indicate phase relations among core flow velocity, core pressure, and wall pressure that are in agreement with experiment.

APPENDIX B: TREATMENT OF TIME-DEPENDENT LOCATION OF UPSTREAM BOUNDARY

The computation of reflection coefficients is motivated by the need to use them as upstream boundary conditions in simple, linearized calculations of the post-shock flow. It is desirable to treat the flow as having a fixed upstream boundary at the time-mean shock location. It is relatively easy to compute conditions immediately behind the shock; however, the shock is not stationary and the results cannot be assigned directly to the time-mean shock location.

Figure B-1 illustrates the pressure distribution prevailing in the channel when the shock is stationary at the time-mean shock position; an instantaneous distribution is also shown. The pre- and post-shock pressures for stationary shocks located at various positions in the channel fall on the static loci as shown. During oscillation around \bar{x}_0 , the post-shock pressure does not lie on the static post-shock pressure locus because of dynamic, nonstationary effects. When the shock is moving upstream, its speed is added to the speed of the approaching flow to obtain the speed relative to the shock, which determines the shock pressure rise. During upstream motion, the post-shock pressure at any location is thus greater than the static value for the same location. The opposite is true during downstream movement, and the post-shock pressure is below the static value. The locus of the post-shock pressures in a dynamic situation can be shown to be an ellipse superimposed on the static locus. The vertical dimensions of the ellipse increase with shock velocity, i.e., with the $(x'_0 \omega)$ product.

Since the calculated post-shock pressures exist on the downstream face of the moving shock, the boundary conditions are known for a sinusoidal boundary in the x - t plane (lower part of Figure B-1). It is desirable to deal with a straight-line boundary in this representation ($x = \bar{x}_0 = \text{const}$), which can be achieved by a linear extrapolation of the instantaneous subsonic pressure distribution to the time-mean shock position, using the slope of the time-mean subsonic pressure distribution as shown in the top part of Figure B-1. The difference between the extrapolated and time-mean value at \bar{x}_0 is the desired equivalent perturbation (p'_e) associated with the stationary \bar{x}_0 location.



GP21-0922-17

Figure B-1. Instantaneous pressure distributions near an oscillating shock in a divergent channel.

This procedure can be applied equally to the velocity perturbations, permitting the computation of admittance ratios and, eventually, the reflection coefficients. The calculations in Reference 14 and the earlier Reference 15 employ this approach, although it is not clarified graphically by either source.